Title

Roles of pre- and post-liquefaction stages in dynamic system response of liquefiable sand retained by a sheet-pile wall

Permalink

https://escholarship.org/uc/item/1r37v116

Authors

Perez, Keith
Reyes, Andres
Taiebat, Mahdi

Publication Date

2023-08-01

DOI

10.1016/j.soildyn.2023.107937

Soil Dynamics and Earthquake Engineering 171 (2023) 107937

Contents lists available at ScienceDirect

Soil Dynamics and Earthquake Engineering

journal homepage: www.elsevier.com/locate/soildyn

Roles of pre- and post-liquefaction stages in dynamic system response of liquefiable sand retained by a sheet-pile wall

Keith Perez, Andrés Reyes, Mahdi Taiebat *

Department of Civil Engineering, University of British Columbia, Vancouver, BC, Canada

ARTICLE INFO

Keywords:
Numerical modeling
Plasticity model
Cyclic liquefaction
Sand
Centrifuge tests
Sheet-pile wall

ABSTRACT

This study examines the dynamic system response of a liquefiable deposit retained by a sheet-pile wall, with emphasis on the roles of pre- and post-liquefaction stages of soil response. A recently developed constitutive model, SANISAND-MSf, is utilized to simulate the pre- and post-liquefaction cyclic response of sands. The model is a stress-ratio controlled, critical state compatible, bounding surface plasticity model, which incorporates the concepts of memory surface and semifluidized state. The model's performance is validated using a combination of cyclic simple shear tests and dynamic centrifuge tests from the LEAP-2020 project. A sensitivity analysis is then conducted by varying the base input motion intensity and duration. The results reveal that the amplitude of equivalent uniform base acceleration in pre-liquefaction correlates well with the timing of liquefaction triggering, and the cumulative absolute velocity of the base acceleration during the post-liquefaction stage correlates well with the post-liquefaction displacements. The study highlights the importance of accurately simulating response in the pre-liquefaction stage for the extent and timing of occurrence of liquefaction, which regulates the remaining intensity and duration of shaking, and in turn, affects the post-liquefaction permanent deformations at the system level.

1. Introduction

In designing geosystems and civil infrastructure within the framework of performance-based earthquake engineering, geotechnical engineers must not only provide an accurate assessment of the occurrence of cyclic liquefaction, but also predict its potentially damaging aftereffects [1]. These consequences can be particularly detrimental for geosystems involving liquefiable soils supported by retaining structures, such as those used to support key infrastructure in port and harbors around the world [2–5]. The reliable prediction of liquefaction-induced lateral spreading and settlement of retained soil is essential for geotechnical engineers designing these systems, as it can significantly affect the serviceability of surrounding infrastructure. To associate the potential occurrence and consequences of cyclic liquefaction to fundamental sand response at the element-level, it is instructive to divide undrained cyclic shearing response into two stages, conveniently termed pre-liquefaction and post-liquefaction. The first instance that the mean effective stress p reaches a value close to zero is often termed initial liquefaction; before and after this instance represent the pre- and post-liquefaction stages of cyclic shearing response. Fig. 1 shows an undrained hollow cylinder cyclic torsional shear test on an isotropically consolidated sample of Toyoura sand to initial mean effective stress $p_0 = 100$ kPa and relative density $D_r \approx 70\%$ subjected to uniform-amplitude cyclic shear stresses with cyclic stress ratio (CSR) $\tau_{cyc}/p_0 = 0.20$. The stress path and shear stress–strain responses are shown in Figs. 1(a) and 1(b), respectively, in different colors to represent the pre- and post-liquefaction stages. Figs. 1(c) and 1(d) showcase the histories of excess pore water pressure ratio r_u and shear strain γ, where the occurrence of initial liquefaction is assumed as the moment r_u exceeds 0.98. At this element-level, pre-liquefaction is characterized by the shear-induced cyclic decrease of p and relatively small shear strains. In post-liquefaction, the stress path nearly locks in a butterfly-shaped orbit, and progressively larger shear strains develop in subsequent loading cycles. The carefully curated cyclic triaxial and hollow cylinder shear tests from Wichtmann and Triantafyllidis [6] and Vargas et al. [7], respectively, support the above observations.

The cyclic resistance of sands in element-level tests is often characterized as the number of uniform cycles or N_{cyc} to reach certain stress- or strain-based criteria, varying from reaching an r_u close to 1.0, e.g., 0.98, to reaching double amplitude shear strains γ^{DA} ranging from 3% to 7.5% [8–10]. Considering a transition between the solid-like and fluid-like states of response [11], the cyclic resistance may vary depending on the criterion used to quantify the cyclic liquefaction. For example, based on Figs. 1(c) and 1(d) the number of cycles to reach

---

* Corresponding author.
E-mail addresses: kcperez@mail.ubc.ca (K. Perez), reyespa@mail.ubc.ca (A. Reyes), mtaiebat@civil.ubc.ca (M. Taiebat).

https://doi.org/10.1016/j.soildyn.2023.107937
Received 6 February 2023; Received in revised form 14 March 2023; Accepted 26 March 2023

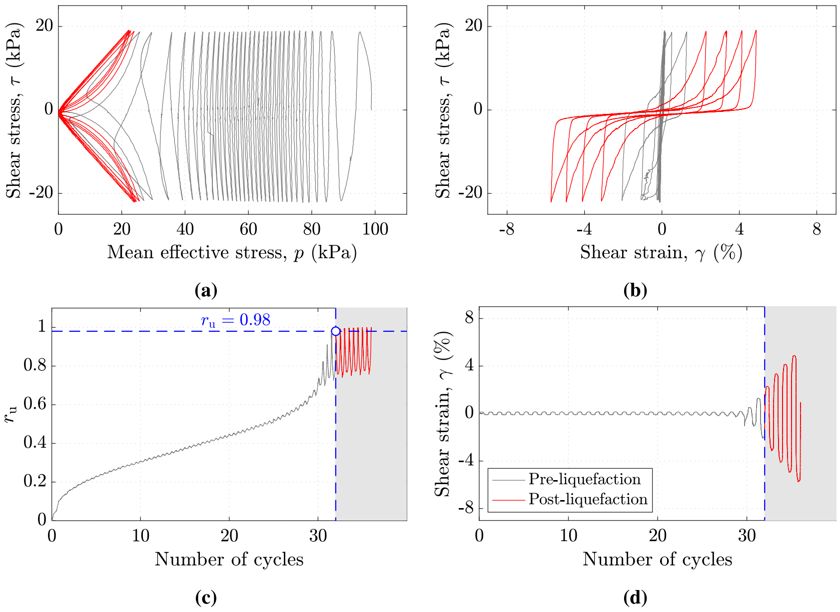

(a) **(b)**

(c) **(d)**

Fig. 1. Pre- and post-liquefaction stages in undrained cyclic simple shear. Experimental data from Umar et al. [12] for isotropically consolidated sample of Toyoura sand with $D_r \approx 70\%$, $p_0 = 100$ kPa, and subjected to a CSR = 0.20.

initial liquefaction in terms of $r_u \geq 0.98$ is around 33 which is very close to the number of cycles to reach $\gamma^{DA} \geq 7.5\%$ that is around 34. This difference is often more pronounced at lower levels of CSR. The number of cycles to reach initial liquefaction is primarily controlled by the shear-induced plastic volumetric response occurring in pre-liquefaction and varies depending on the material state and the amplitude of cyclic shearing. The influencing factors on the shear strains developed in the post-liquefaction are not studied as extensively as those affecting the pre-liquefaction response.

Reliable numerical simulations of cyclic liquefaction must use soil constitutive models that are capable of capturing the most important features of the pre- and post-liquefaction responses for a wide range of amplitudes of cyclic shear stress. Several sand constitutive models have been developed with different strategies to simulate cyclic liquefaction. The strain space multiple mechanism cocktail glass model proposed by Iai et al. [13] has been updated in Iai et al. [14] by using a new stress-dilatancy relationship which improves the prediction of cyclic undrained response under isotropic and anisotropic initial states. Within the multi-yield surface plasticity [15] framework, the PDMY03 model by Khosravifar et al. [16] modified the flow rule of the model by Elgamal et al. [17] to directly associate liquefaction triggering to cyclic resistance relationships. With respect to bounding surface plasticity [18], the PM4SAND of Boulanger and Ziotopoulu [19] and the P2P model by Cheng and Detournay [20] made corresponding enhancements to the plastic modulus and dilatancy of the reference model by Dafalias and Manzari [21] for an improved simulation of cyclic liquefaction resistance. Wang et a. [22] and Yu et al. [23] modified the CycLiq model of Wang et al. [24] by proposing a modified dilatancy rate to improve the predictive capabilities for relatively low values of CSR. More recently, Yang et al. [25] proposed SANISAND-MSf by introducing two constitutive ingredients for the Dafalias and Manzari [21] reference model, which provide the flexibility necessary to capture both pre- and post-liquefaction responses in undrained cyclic shearing for a wide range of cyclic stress amplitudes, mean effective stresses, and relative densities. The above summary only presents some of the several recent developments related to the constitutive modeling of cyclic liquefaction. These developments in constitutive modeling are often validated against relationships between CSR and N_{cyc}, namely cyclic resistance curves, which summarize the combined response of pre- and post-liquefaction stages in laboratory tests. This usually means that a user must choose a set of constants that can capture accurately either (a) the number of cycles in the pre-liquefaction stage, (b) the large cyclic shear strains in post-liquefaction, or (c) a compromised response between these (a) and (b). However, the consequences of these choices in the analysis of boundary value problems are unclear, particularly when determining the timing of the occurrence of cyclic liquefaction and the ensuing development of cyclic deformations.

The primary objective of this study is to evaluate the roles of the pre- and post-liquefaction stages on the system response of a liquefiable deposit supported by a sheet-pile wall. This type of retaining structure is commonly used to support potentially liquefiable soils in port and harbor facilities. Coupled dynamic numerical modeling frameworks together with the state-of-the-art soil constitutive models for simulating cyclic liquefaction provide valuable insights into the seismic performance of these types of soil–structure systems [26,27]. This has been the main philosophy of the numerical modeling component of the Liquefaction Experiments and Analysis Projects (LEAP), a series of international collaborative efforts to analyze the dynamic response and liquefaction of soil–structure systems [e.g., 28]. In particular, LEAP-2020 exercise was focused on modeling the seismic-induced liquefaction response of a soil-sheet-pile wall system. In this paper, the SANISAND-MSf constitutive model is first calibrated using an extensive database of element-level tests and then validated by nonlinear coupled dynamic analysis of a series of centrifuge experiments developed as part of LEAP-2020. The validated predictive capabilities are then used in a sensitivity analysis where the same system is subjected to base input motions with a variety of maximum accelerations and durations. This combination allowed for evaluating cases where the system was subjected to a wide range of cyclic stress amplitudes and number of loading cycles. The significance of accurately simulating the pre- and post-liquefaction stages is illustrated by determining the timing of the occurrence of cyclic liquefaction, the displacements that develop after triggering, and how the system displacements correlate with shaking intensity and duration.

2. Numerical framework

2.1. Computational framework

The computational platform used in this study is the nonlinear finite difference software program FLAC^{3D} [29]. This program solves the complete set of the dynamic equation of motion using an explicit time-integration scheme. It includes coupled solid-pore fluid interaction, relevant boundary conditions to dynamic problems, and the possibility of incorporating user-defined constitutive models, making it well suited for dynamic stress-deformation and liquefaction-related analyses. The continuous three-dimensional medium can be discretized and represented by hexahedral zones, also called brick elements, that may be adjusted to fit the target geometry of the simulated domain. Each hexahedral zone consists of two overlying sets of five constant strain rate tetrahedral subzones, whose vertices coincide with the ones of the zone. This discretization does not generate unwanted hour-glassing modes of deformation. However, when used within the plasticity framework, these elements do not provide enough modes of deformation, e.g., they cannot deform individually without a change of volume. To overcome the overly stiff behavior of uniform strain tetrahedra during plastic flow, the program adopts a so-called mixed-discretization process, in which the mean effective stress and volumetric strain components are averaged over the subzones of each zone, while the deviatoric stress and strain components are treated separately for each subzone. During each time step, the constitutive model for stress integration is called once per subzone to calculate the new stresses for the given strain increments. The mean stresses and volumetric strains are then averaged within the entire zone after the stress integration is completed in all subzones. Accommodating this process requires special treatments for scalar and tensorial internal variables used in the integration of elastoplastic constitutive models, including the SANISAND-MSf model, following the details presented in Barrero [30].

Two relevant analysis configurations in FLAC^{3D} are the fluid-mechanical interaction and the dynamic setting. The formulation of coupled deformation-fluid diffusion processes is done within the framework of the quasi-static Biot's theory and can be applied to problems involving single-phase Darcy flow in a porous medium. For the effective stress calculation in each step, the total stress increment due to pore-pressure change arising from mechanical volumetric strain is evaluated in a mechanical loop, and that arising from the fluid flow is evaluated in a flow loop. Zone pore pressures are calculated by averaging from the gridpoint values, and used to derive effective stresses for use in the constitutive models. In the dynamic analysis setting, the explicit finite difference scheme of the program is applied to solve the full equations of motion using lumped grid point masses derived from the real density of surrounding zones. The dynamic feature can be coupled with the fluid-mechanical interaction feature, making the software capable of modeling dynamic pore water pressure generation in the transient loading process. In its extreme case, this may lead to liquefaction.

2.2. Constitutive model

Dafalias and Manzari [21] introduced a stress-ratio controlled, critical state compatible, bounding surface plasticity model, often referred to as DM04, which formed the basis of what was later named the SANISAND class of models [31]. The DM04 model is well-established as it has been widely used over the years for a variety of liquefaction related problems (e.g., Taiebat et al. [32], Ramirez et al. [33], Ghofrani and Arduino [34], Reyes et al. [35]). The SANISAND class includes various extensions (e.g., Li and Dafalias [36], Dafalias and Taiebat [37], Petalas et al. [38,39]), each addressing different aspects of the mechanical response of sands. In this paper, the most recent extension by Yang et al. [25], named SANISAND-MSf (S-MSf), is used. The S-MSf model follows the basic framework of the reference model DM04 and adds two novel constitutive ingredients to improve the undrained cyclic shear response. These key ingredients derived the name of S-MSf for the model, with M standing for 'memory surface' and Sf for 'semifluidized state'.

The S-MSf operates primarily based on five conical surfaces, as schematically illustrated in the 3D stress principal axes space in Fig. 2.

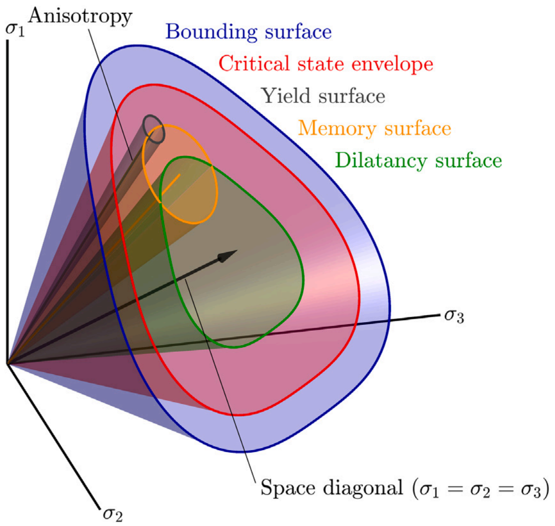

Fig. 2. Schematic illustration of the SANISAND-MSf surfaces in the 3D stress principal axes space (modified from Medicus and Taiebat [40]).

The first four surfaces are the same as those in the DM04: a yield surface (YS) centered at the back-stress ratio $\boldsymbol{\alpha}$ that obeys kinematic hardening and has a small opening size proportional to model constant m, and three other Lode angle-dependent and origin-concentric surfaces: bounding surface (BS), critical state surface (CS), and dilatancy surface (DS). In contrast to the YS, the opening sizes of BS and DS evolve through the course of loading depending on state parameter $\psi = e - e_c$, i.e., the distance between the current void ratio and the critical void ratio at the current mean stress p. Following a mapping rule, the distance between the YS and BS controls the plastic modulus, and the distance between the YS and DS controls the dilatancy. The fifth surface is a memory surface (MS) centered at the back-stress ratio $\boldsymbol{\alpha}^{\mathrm{M}}$ that obeys kinematic hardening and has an opening size proportional to the internal variable m^{M} that obeys isotropic hardening, The summary of the model equations in their multiaxial stress–strain forms and the relevant model constants are presented in Table 1.

The role of MS, which is a modification from earlier propositions [41,42], is to control the plastic stiffness in the pre-liquefaction stage of cyclic loading. This is to remedy a deficiency of DM04 in estimating the cyclic liquefaction resistance at different CSR levels. The MS is allowed to grow for stress ratios within the DS, and it has a fast-shrinking mechanism only during dilation. This latest feature bounds the effect of the MS in the pre-liquefaction response. The effect on the plastic modulus is through a distance b^{M} between MS and YS, and regulated by model constants μ_0 and u, according to:

$$k_{\mathrm{M}} = \exp\left\{\left[\mu_0/(\|\boldsymbol{\alpha}_{\mathrm{in}}\|^u + \varepsilon)\right](b^{\mathrm{M}}/b_{\mathrm{ref}})^w\right\} \tag{1}$$

where the discrete internal variable $\boldsymbol{\alpha}_{\mathrm{in}}$ is the back stress ratio at the last stress ratio rate reversal, b_{ref} is the bounding surface size along $\mathbf{n}$ used for normalization, and ϵ and w are model constants with default values of 0.01 and 2, respectively. The norm of $\boldsymbol{\alpha}_{\mathrm{in}}$ is used as a proxy for the cyclic shear stress ratio amplitude, and together with the b^{M} allows for capturing the undrained cyclic resistance at different cyclic shear stress amplitudes. The coefficient k_{M} affects plastic modulus through h via b_0.

The concept of Sf state, introduced by Barrero et al. [43], refers to the state of granular material when the p is very small, namely when $p < p_{\mathrm{th}}$ where the threshold mean effective stress p_{th} is a model constant with the default value 10 kPa. An internal state variable named the Strain Liquefaction Factor (SLF) and symbolized by ℓ is introduced, whose purpose is to induce stiffness and dilatancy degradation

Table 1

SANISAND-MSf model formulation and associated model constants.

Description	Multiaxial equations*	Constants†
Elastic relations	$\dot{\mathbf{e}}^{\mathrm{e}} = \dot{\mathbf{s}}/(2G);\ \dot{\varepsilon}_{\mathrm{v}}^{\mathrm{e}} = \dot{p}/K$	
Plastic relations	$\dot{\mathbf{e}}^{\mathrm{p}} = \langle L\rangle \mathbf{R}^{*};\ \ \dot{\varepsilon}_{\mathrm{v}}^{\mathrm{p}} = \langle L\rangle D$	
Hypoelastic moduli	$G = G_0 p_{\mathrm{at}}(2.97 - e)^2/(1+e)(p/p_{\mathrm{at}})^{1/2}$	G_0
	$K = 2(1+\upsilon)/\left[3(1-2\upsilon)G\right]$	υ
Critical state line	$e_c = e_c^{\mathrm{ref}} - \lambda_c (p/p_{\mathrm{at}})^{\xi}$	$e_c^{\mathrm{ref}},\ \lambda_c,\ \xi$
Yield surface	$f = \sqrt{(\mathbf{s} - p\boldsymbol{\alpha}):(\mathbf{s} - p\boldsymbol{\alpha})} - \sqrt{2/3}pm = 0$	m
Deviatoric flow rule	$\mathbf{R}^{*} = x_{\alpha}^2 \mathbf{n} + (1 - x_{\alpha}^2)\mathbf{R}'/\lVert \mathbf{R}' \rVert$	
	$\mathbf{R}' = B\mathbf{n} - C\left[\mathbf{n}^2 - (1/3)\mathbf{I}\right]$	
	$\mathbf{n} = (\mathbf{r} - \boldsymbol{\alpha})/\lVert \mathbf{r} - \boldsymbol{\alpha} \rVert;\ \ \mathbf{n}_{\alpha} = \boldsymbol{\alpha}/\lVert \boldsymbol{\alpha} \rVert$	
	$B = 1 + 3(1-c)/(2c)g(\theta,c)\cos 3\theta\ ;\quad C = 3\sqrt{3/2}(1-c)g(\theta,c)/c$	
	$g(\theta,c) = 2c/\left[(1+c) - (1-c)\cos 3\theta\right]$	c
	$\cos 3\theta = \sqrt{6}tr(\mathbf{n}^3);\ \ \cos 3\theta = \sqrt{6}tr(\mathbf{n}_{\alpha}^3)$	
	$x_{\alpha} = \langle \alpha_{\theta_{\alpha}}^{b} - \lVert \boldsymbol{\alpha} \rVert \rangle/\alpha_{\theta_{\alpha}}^{\mathrm{b}};\quad \alpha_{\theta_{\alpha}}^{\mathrm{b}} = \sqrt{2/3}\left[g(\theta_{\alpha},c)M\exp(n^{\mathrm{b}}\langle -\psi\rangle) - m\right]$	
Dilatancy	$D = A_0' g(\theta,c)^{-n_g}(1 + \langle \mathbf{z}:\mathbf{n}\rangle)\left[(\boldsymbol{\alpha}_{\theta}^{\mathrm{d}} - \boldsymbol{\alpha}):\mathbf{n}\right] k_{\mathrm{Sf}}$	$A_0',\ n_g$
	$\dot{\mathbf{z}} = -c_z\langle -\dot{\varepsilon}_{\mathrm{v}}^{\mathrm{p}}\rangle(z_{max}\mathbf{n} + \mathbf{z})$	$c_z,\ z_{\mathrm{max}}$
Kinematic hardening	$\dot{\boldsymbol{\alpha}} = \langle L\rangle(2/3)h(\boldsymbol{\alpha}_{\theta}^{\mathrm{b}} - \boldsymbol{\alpha})$	
	$h = b_0/\left[(\boldsymbol{\alpha} - \boldsymbol{\alpha}_{\mathrm{in}}):\mathbf{n}\right]$	
	$b_0 = G_0 h_0' g(\theta,c)^{-n_g}(1 - c_h e)(p/p_{\mathrm{at}})^{-1/2} k_{\mathrm{M}} k_{\mathrm{Sf}}$	$h_0',\ c_h$
Image point on BS	$\boldsymbol{\alpha}_{\theta}^{\mathrm{b}} = \sqrt{2/3}\left[g(\theta,c)M\exp(n^{\mathrm{b}}\langle -\psi\rangle) - m\right]\mathbf{n}$	$M,\ n^{\mathrm{b}}$
Image point on DS	$\boldsymbol{\alpha}_{\theta}^{\mathrm{d}} = \sqrt{2/3}\left[g(\theta,c)M\exp(n^{\mathrm{d}}\psi) - m\right]\mathbf{n}$	n^{d}
Memory surface	$f^{\mathrm{M}} = \sqrt{(\boldsymbol{\alpha}_{\theta}^{\mathrm{M}} - \boldsymbol{\alpha}^{\mathrm{M}}):(\boldsymbol{\alpha}_{\theta}^{\mathrm{M}} - \boldsymbol{\alpha}^{\mathrm{M}})} - \sqrt{2/3}m^{\mathrm{M}} = 0$	
	$k_{\mathrm{M}} = \exp\left\{\left[\mu_0/(\lVert \boldsymbol{\alpha}_{\mathrm{in}} \rVert^{u} + \varepsilon)\right](b^{\mathrm{M}}/b_{\mathrm{ref}})^{w}\right\}$	$\mu_0,\ u,\ \varepsilon = 0.01,\ w = 2$
	$b^{\mathrm{M}} = (\boldsymbol{\alpha}_{\theta}^{\mathrm{M}} - \boldsymbol{\alpha}):\mathbf{n}\ ;\quad b_{\mathrm{ref}} = (\boldsymbol{\alpha}_{\theta}^{\mathrm{b}} - \boldsymbol{\alpha}_{\theta+\pi}^{\mathrm{b}}):\mathbf{n}$	
Image point on MS	$\boldsymbol{\alpha}_{\theta}^{\mathrm{M}} = \alpha^{\mathrm{M}} + \sqrt{2/3}m^{\mathrm{M}}\mathbf{n}$	
	$\dot{\boldsymbol{\alpha}}^{\mathrm{M}} = \langle L\rangle(2/3)h^{\mathrm{M}}(\boldsymbol{\alpha}_{\theta}^{\mathrm{b}} - \boldsymbol{\alpha}_{\theta}^{\mathrm{M}})$	
	$\dot{m}^{\mathrm{M}} = \langle L\rangle\left[\sqrt{2/3}c_{\mathrm{c}}h^{\mathrm{M}}\langle(\boldsymbol{\alpha}_{\theta}^{\mathrm{b}} - \boldsymbol{\alpha}_{\theta}^{\mathrm{M}}):\mathbf{n}\rangle - m^{\mathrm{M}}/\varsigma\lvert(\boldsymbol{\alpha}_{\theta}^{\mathrm{b}} - \boldsymbol{\alpha}_{\theta}^{\mathrm{M}}):\mathbf{n}\lvert\langle -D\rangle\rvert\right]$	$c_{\mathrm{c}} = 1,\ \varsigma = 0.00001$
	$h^{\mathrm{M}} = \left\{h + \sqrt{3/2}(m^{\mathrm{M}}/\varsigma)\mathrm{sgn}\left[(\boldsymbol{\alpha}_{\theta}^{\mathrm{b}} - \boldsymbol{\alpha}_{\theta}^{\mathrm{M}}):\mathbf{n}\right]\langle -D\rangle\right\}/\left\{1 + c_c\mathcal{H}\left[(\boldsymbol{\alpha}_{\theta}^{\mathrm{b}} - \boldsymbol{\alpha}_{\theta}^{\mathrm{M}}):\mathbf{n}\right]\right\}$	
Semifluidized state	$\dot{\ell} = \langle L\rangle\left[c_{\ell}\langle 1 - p_{\mathrm{r}}\rangle(1 - l)^{n_{\ell}}\right] - c_r\ell\lvert\dot{\varepsilon}_{\mathrm{v}}\rvert;\quad p_r = p/p_{\mathrm{th}}$	$c_{\ell},\ n_{\ell} = 8,\ c_{\mathrm{r}},\ p_{\mathrm{th}} = 10$ kPa
	$k_{\mathrm{Sf}} = \left(1 - \langle 1 - p_{\mathrm{r}}\rangle\right)^{x\ell} + f_{\ell}$	$x, f_{\ell} = 0.01$

* Tensor-value quantities are shown by bold face characters and the symbol : means the trace of the product of adjacent tensors.

† Some constants have indicated default numerical values.

only within the Sf state. The ℓ evolves from its minimum value 0 to maximum value 1 only when $p_{\mathrm{r}} = p/p_{\mathrm{th}} < 1$ according to:

$$\dot{\ell} = \langle L\rangle\left[c_{\ell}\langle 1 - p_{\mathrm{r}}\rangle(1 - \ell)^{n_{\ell}}\right] - c_{\mathrm{r}}\ell\lvert\dot{\varepsilon}_{\mathrm{v}}\rvert \tag{2}$$

where c_{ℓ} is a model constant controlling the evolution rate of ℓ and n_{ℓ} is a model constant with the default value 8. The rate term of Eq. (2) is zero for undrained loading where $\dot{\varepsilon}_{\mathrm{v}} = 0$, and leads ℓ towards zero during drained loading inside or outside the semifluidized state with a pace controlled by the model parameter c_{r}. This last feature would be important in the modeling of re-liquefaction, but in the absence of relevant data for calibration it is deactivated by setting $c_{\mathrm{r}} = 0$ in the present study. The role of the SLF is to decrease the plastic shear modulus and dilatancy by adjusting the levels of b_0 and D, respectively, according to:

$$k_{\mathrm{Sf}} = \left(1 - \langle 1 - p_{\mathrm{r}}\rangle\right)^{x\ell} + f_{\ell} \tag{3}$$

where x is a model constant controlling the maximum degradation of b_0 and D and consequently the maximum level of cyclic shear strain amplitude, and f_{ℓ} is another model constant with the default value 0.01. As was the case for k_{M}, k_{Sf} affects h and K_{p} through b_0, as listed in Table 1. The same argument applies to dilatancy. Observe that outside the Sf state $p_{\mathrm{r}} > 1$ and $k_{\mathrm{Sf}} = (1 + f_{\ell})$, and considering the very small value of $f_{\ell} = 0.01$, b_0 and D are not affected by ℓ.

The roles of the MS and Sf ingredients with respect to the reference model DM04 are illustrated in Fig. 3. Figs. 3(a,d) showcase the undrained hollow cylinder cyclic torsional shear test previously presented in Fig. 1. Simulations using S-MSf are shown in Figs. 3(c,f), while comparative results using DM04 are presented in Fig. 3(b,e), in which the S-MSf modification to the reference model DM04 are deactivated. The DM04 overestimates the pace of cyclic reduction of the mean stress, i.e., it overestimates the pace of cyclic increase of pore water pressure, leading to an underestimation of the cyclic liquefaction resistance for this level of CSR. In addition, the DM04 shows freezing of the shear stress–strain loops in the post-liquefaction stage when the stress path goes on the 'butterfly' orbit, leading to considerable underestimation of the post-liquefaction cyclic shear strain accumulation. Tuning the DM04 model constants may slightly improve the cyclic liquefaction resistance for a certain CSR but would negatively compromise the response at other levels of CSR, and without addressing the post-liquefaction strain accumulation. The simulated response using the S-MSf model builds on the framework of DM04 and provides additional degrees of freedom to overcome the aforementioned limitations. More specifically, the S-MSf can adequately simulate the shear-induced demise of p in the pre-liquefaction as shown in Fig. 3(c), and the progressive development of large cyclic shear strains in the post-liquefaction as shown in Fig. 3(f).

Figs. 3(g,h) further show the histories of the model internal variables b^{M} and ℓ, respectively. In particular, as cyclic shearing progresses and while the stress ratio remains within the dilatancy surface, the MS expands, increasing the distance b^{M} as shown in Fig. 3(g). The augmented b^{M} exponentially increases the k_{M} following Eq. (1). This, in turn, enhances the plastic stiffness, which results in a slower reduction of p. When the stress path reaches the dilation phase after cycle 28, the MS starts shrinking rapidly, which results in a decrease of the b^{M}, bringing it down to zero at around cycle 30, as depicted in Fig. 3(g). Beyond this point, as long as the stress path stays on the 'butterfly' orbit, b^{M} will remain at zero and will have no further stiffening effect on the post-liquefaction response. Similarly, Fig. 3(h) reproduces the history of ℓ. As outlined in Eq. (2), ℓ only starts to increase when $p_{\mathrm{r}} < 1$, which occurs after cycle 30. The progressive increase of ℓ degrades the plastic deviatoric stiffness of the model within the Sf state. The enhanced controls of the excess pore water pressure build-up in the pre-liquefaction stage, and cyclic shear strain accumulation in the post-liquefaction stage, are further illustrated in Figs. 3(i,j), showing the histories of excess pore water pressure ratio r_{u} and shear strain γ.

3. Validation of numerical modeling approach

The combined use of the computational framework and constitutive model described in Section 2 is validated in this section. The validation

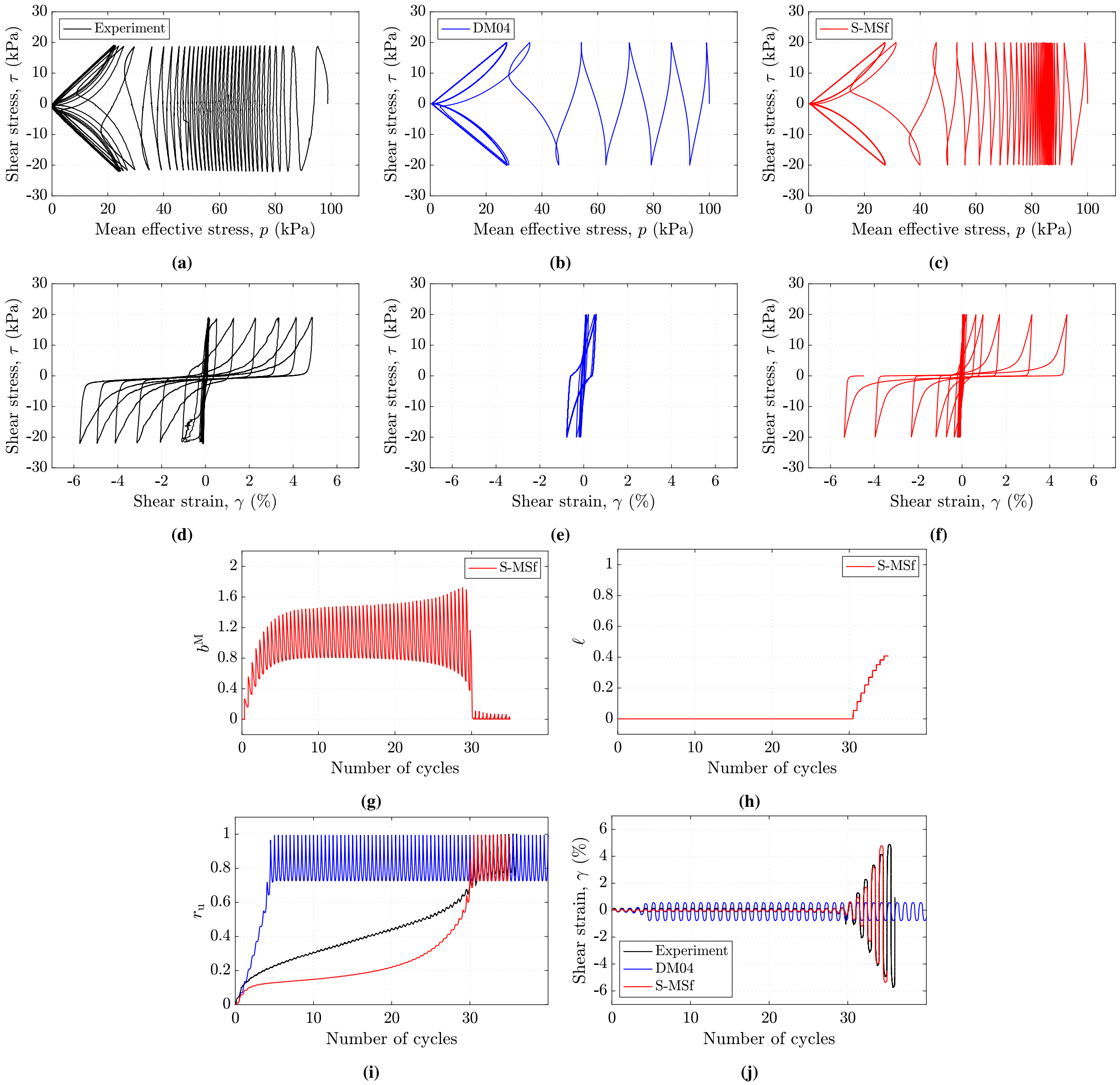

Fig. 3. Simulation of undrained cyclic torsional shear tests (experimental data from [12]) on an isotropically consolidated sample of Toyoura sand with $D_r \approx 70\%$, $p_0 = 100$ kPa, and subjected to a CSR = 0.20, illustrating the roles of the constitutive ingredients memory surface via b^M and semifluidized state via ℓ in elevating the simulation capabilities of S-MSf compared to DM04.

targeted the seismic-induced system response observed in a series of centrifuge experiments consisting of a saturated sand deposit supported by a sheet-pile wall. In these experiments, liquefaction-induced deformations and soil–structure interaction between sand and sheet-pile wall control the overall dynamic response. This section first describes the element-level test data used to characterize the sand and calibrate the S-MSf model constants. Then the key information related to the target centrifuge tests is presented, followed by details of the numerical model setup of those centrifuge tests in FLAC^{3D}. Finally, details of the validation results for the numerical models of the centrifuge tests are presented.

3.1. Calibration of constitutive model

The designated soil used in the validation study is Ottawa F65 sand. This anthropic material is a clean, poorly graded soil produced by US Silica, consisting of 99% silica and around 1% of fines, and with subrounded particle shape. Ottawa F65 sand has been extensively characterized, primarily within the context of the collaborative international benchmarking endeavor LEAP. The main objective of LEAP has been exploiting the combined use of high-quality laboratory experiments, advanced centrifuge testing, and numerical modeling, with a focus on liquefaction-related problems [28]. Ottawa F65, as noted by Kutter et al. [44], has maximum and minimum densities of 1 757 and 1 491 kg/m^3, respectively, a specific gravity G_s of 2.65, and hydraulic conductivity ranging from 0.01 to 0.016 m/s, depending on its void ratio. The undrained cyclic shear response of this sand has been studied through conventional triaxial, direct simple shear, and hollow cylinder torsional shear tests [e.g., 7,45,46]. Relevant works documenting and further enriching the characterization of the cyclic response of Ottawa F65 sand are those of Kutter et al. [44] and El Ghoraiby and Manzari [47].

In this study, selected undrained hollow cylinder cyclic torsional shear (HCCTS) tests by Vargas et al. [7] were used to characterize the undrained cyclic resistance. The tests were conducted on isotropically consolidated ($K_0 = 1$) samples of Ottawa F65 sand with $D_r = 50$, 60% and $p_0 = 100$ kPa. Under undrained conditions, the samples were subjected to uniform cyclic shear stress with different values of CSR,

Table 2
SANISAND-MSf calibrated model constants for Ottawa F65 sand.

Model constant	Symbol	Value
Elasticity	G_0	125
	ν	0.05
Critical state	M	1.26
	c	0.735
	e_c^{ref}	0.78
	λ_c	0.0287
	ξ	0.7
Yield surface	m	0.01
Dilatancy	n^{d}	2.50
	A_0'	0.626
	n_g	0.9
Fabric dilatancy	$z_{\max}$	15
	c_z	2000
Kinematic hardening	n^{b}	3.5
	h_0'	4.6
	c_h	0.968
Memory surface	μ_0	1.99
	u	1.32
Semifluidized state	x	3.5
	c_ℓ	35

covering a range between 0.09 and 0.20. Additionally, the data of constant-volume cyclic direct simple shear tests (CDSS) by El Ghoraiby and Manzari [48] was used to evaluate the response of Ottawa F65 under initial and loading conditions resembling those experienced by soil in the LEAP centrifuge experiments. This latter set of data was on anisotropically consolidated ($K_0 \neq 1$) samples of Ottawa F5 sand with $\mathrm{D_r} = 66\%$, $\sigma_{\mathrm{v0}} = 30$ kPa and a mean cyclic shear stress or the so-called initial shear stress $\tau_{\mathrm{mean}} = 2.6$ kPa. Unlike conventional cyclic tests, these samples were subjected to 15 non-uniform cycles of shearing, with different maximum values of CSR. These initial and loading conditions were expected to be representative of the typical initial states and shaking levels in the centrifuge experiments conducted within LEAP.

The S-MSf model constants were calibrated primarily to capture the cyclic resistance of Ottawa F65 sand. The list of calibrated model constants is presented in Table 2, organized in terms of their function within the constitutive framework of the model. The model constants shared with the reference model DM04 were calibrated following the procedure outlined in Taiebat et al. [32]. In particular, the constants associated with elasticity, critical state, yield surface, dilatancy, kinematic hardening, and fabric dilatancy were inherited from the works of Ramirez et al. [33] and Barrero et al. [43]. The value of $n^{\mathrm{b}} = 3.5$ used in this study was suggested by Reyes et al. [49] to better control the shear strain accumulation in the presence of non-zero mean shear stresses.

The model constants associated with the MS, i.e., μ_0 and u, and those associated with the Sf state, i.e., x and c_ℓ, were determined based on results of the undrained HCCTS tests performed by Vargas et al. [7]. Fig. 4 presents a subset of HCCTS test results and their corresponding simulations with DM04 and S-MSf. In the pre-liquefaction stage, the progressive evolution of the undrained stress path simulated by S-MSf is in better agreement with the corresponding experiments for low CSR levels (i.e., 0.099, 0.127) because of the incorporation of the MS. Additionally, incorporating the Sf has substantially improved the accumulation of stress–strain loops during the post-liquefaction stage, bringing them much closer to the experimental data for all CSR levels. However, the simulated hysteresis loops' magnitudes are somewhat smaller than those observed in the experiment, which is believed to be attributed to the fabric dilatancy formulation of the model. Overall, the incorporation of the Sf has significantly enhanced the model's ability to capture the post-liquefaction behavior. As detailed in Yang et al. [25], the μ_0 and u primarily control the position and slope of the cyclic resistance curve in the plot of CSR vs. the number of cycles to reach liquefaction. Consequently, μ_0 was determined first, considering this curve's position for the highest CSR values in the experimental dataset. Subsequently, u, which primarily affects the response at the lowest values of CSR, was determined for adjusting the slope of the CSR–N curve. Then, the model constants related to the Sf constitutive ingredient, namely x and c_ℓ, were determined to capture the post-liquefaction shear strain amplitudes observed in the tests by Vargas et al. [7]. As illustrated in Reyes et al. [49], x and c_ℓ control the maximum amplitude of shear strains and pace of strain generation in the Sf state, respectively. It is important to highlight that the MS, through the choices of μ_0 and u, does not impact the calibration of x and c_ℓ as the effect of MS vanishes in the post-liquefaction stage. This intended design of the constitutive equations in S-MSf is a convenient feature in the calibration process as it provides a much-needed degree of flexibility to capture the response in both pre- and post-liquefaction stages, and to capture cyclic resistance for different liquefaction criteria, i.e., based on reaching certain levels of r_{u} or shear strain. Fig. 5 summarizes the overall performance of S-MSf in capturing cyclic resistance for the experiments from Vargas et al. [7]. The simulated response using reference model DM04 is also presented. Here, two criteria are chosen to produce the CSR-$\mathrm{N_{cyc}}$ curve: $r_{\mathrm{u}} = 0.98$ in Fig. 5(a) and $\gamma^{\mathrm{DA}} = 7.5\%$ or reaching 7.5% double amplitude of cyclic shear strain in Fig. 5(b). Fig. 5(c) shows the number of cycles between reaching $r_{\mathrm{u}} = 0.98$ and $\gamma^{\mathrm{DA}} = 7.5\%$, which can be considered at the ones in an early part of the post-liquefaction stage. Note that no cyclic resistance curve is drawn for the criteria of $\gamma^{\mathrm{DA}} = 7.5\%$ when using DM04 since the reference model is incapable of developing such large strains in simple shear tests subjected to symmetric cyclic shearing.

El Ghoraiby and Manzari [48] carried out a series of CDSS tests on K_0 consolidated samples of Ottawa F65 sand with non-zero static shear stress. The samples were subjected to ramped sinusoidal shearing with different levels of peak CSR while maintaining the mean cyclic shear stress. The performances of the calibrated DM04 and S-MSf models were also evaluated against these tests. The comparison for selected cases with $\mathrm{D_r} = 66\%$ are presented in Fig. 6. In particular, Fig. 6(a) shows the experimental stress path and stress–strain response for the test with $\sigma_{\mathrm{v0}} = 30$, $\tau_{\mathrm{mean}} = 2.6$ kPa, and peak CSR $= 0.42$, and Figs. 6(c,e) show the corresponding DM04 and S-MSf simulations, respectively. Similarly, Figs. 6(b,d,f) show the experimental results and the corresponding DM04 and S-MSf simulations for the case with $\sigma_{\mathrm{v0}} = 40$, $\tau_{\mathrm{mean}} = 3.5$ kPa, and peak CSR $= 0.31$. The two models show a similarly reasonable response in terms of the evolution of the stress path. While both models show non-symmetric accumulation of shear strains towards the direction of τ_{mean}, the magnitude of the accumulated strain for the S-MSf model is larger and in better agreement with those of the experiment, which originates from the semifluidized state formulation in the post-liquefaction stage of response.

3.2. Description of numerical model

3.2.1. Centrifuge tests

The centrifuge tests used to validate the numerical model in this study were those conducted as part of the recent LEAP-2020 [50–54]. These tests were also used recently in several numerical modeling studies with a focus on the use of the state-of-the-art constitutive models [e.g.,55–58]. The centrifuge setup consisted of a submerged two-layered deposit of Ottawa F65 sand supported by a sheet-pile wall. Fig. 7 shows the schematic setup of the target LEAP-2020 centrifuge tests in the prototype dimensions, with an overall length, height, and width of 20.0, 5.0, and 8.5 m, respectively. A total of ten centrifuge tests, conducted at various centrifuge facilities as listed in Table 3, were selected for this study. The top and bottom sand layers of the 'backfill' and 'toefill' were deposited at $\mathrm{D_r}$ ranging 55%–76% and 65%–93%, respectively. The sheet-pile walls were made of aluminum with a Young's modulus of $E = 69$ GPa. In the prototype scale, the walls had a thickness ranging from 5 to 12 cm and an effective length of 4.5 m measured from the backfill surface, which included an embedment of

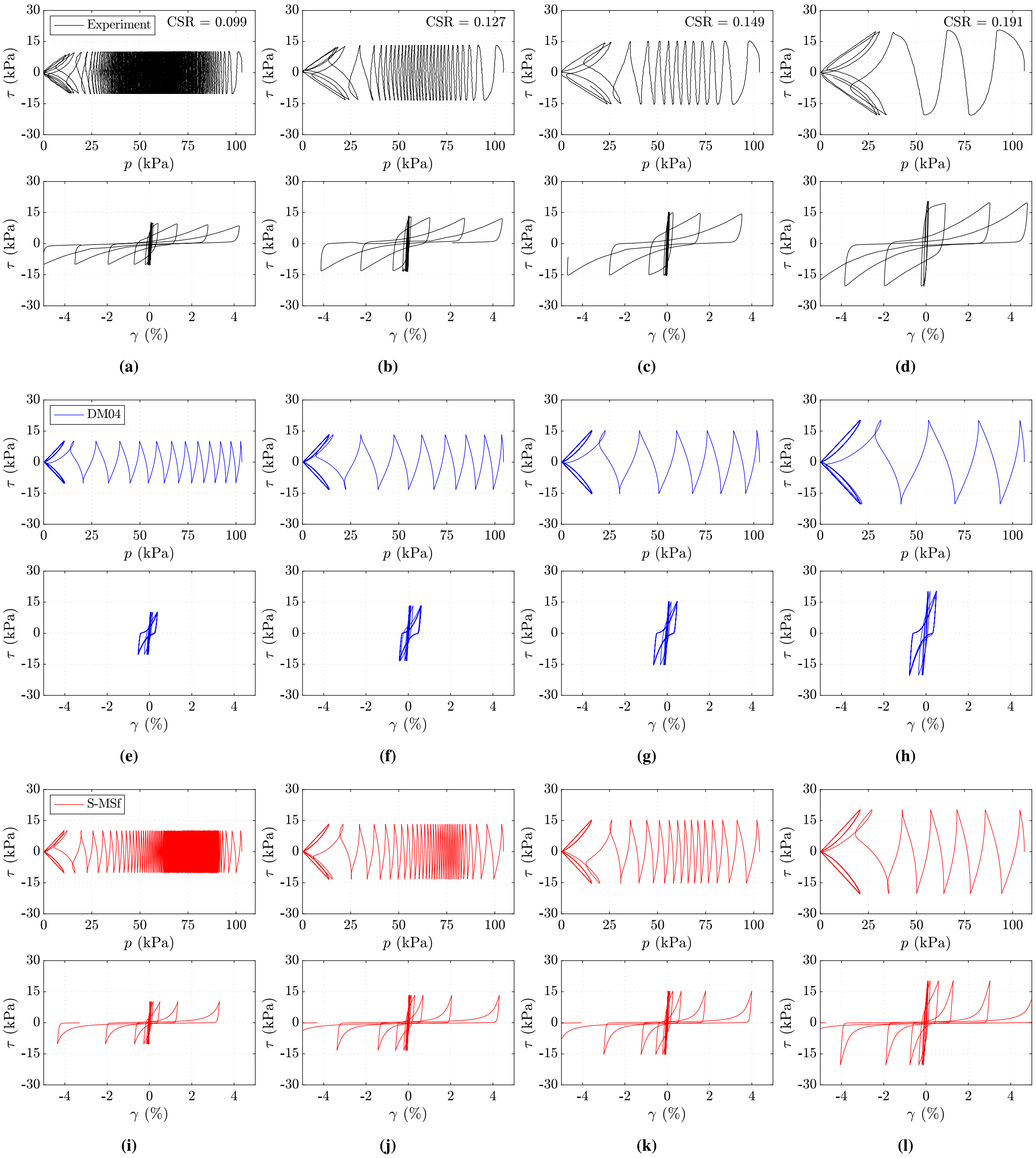

(a) (b) (c) (d)

(e) (f) (g) (h)

(i) (j) (k) (l)

Fig. 4. Stress path and stress–strain response from undrained hollow cylinder cyclic torsional tests and corresponding simulations on isotropically consolidated samples of Ottawa F65 sand with $D_r = 50\%$ and $p_0 = 100$ kPa: (a-d) experimental data from Vargas et al. [7] at CSR = 0.099, 0.127, 0.149, and 0.19, respectively; (e-h) DM04 simulations, and (i-l) S-MSf simulations.

0.5 m in the bottom sand layer. Relevant details of the centrifugal acceleration, relative densities of the top and bottom sand layers, and thickness of sheet-piles for all centrifuge tests are presented in Table 3.

Each centrifuge model was first built in dry conditions, and then saturated to achieve fully submerged conditions; the wall was constrained against lateral movement during these stages. The lateral constraint of the wall was then removed, and centrifugal acceleration was exerted on the model to achieve the target self-weight at the prototype scale. The system was then subjected to the target excitations at the base of the centrifuge box. Fig. 7 further presents selected locations of the instrumentation used to monitor the system response in the subsequent validation stage in this study. Within the soil body, these sensors included horizontal accelerometers (AH), pore water pressure transducers (P), and surface markers. Descriptors 'B', 'M', and 'W' were used in labeling the sensor arrays in the far back of the backfill, middle of the container, and closer to the wall in the backfill. Similarly, 'FWB' is used for labeling the sensors in the toefill or front of the wall. Also, linear variable differential transducers (LVDT) were installed at two elevations on the hanging part of the wall above the backfill surface, to monitor the displacements of the top of the sheet-pile wall. The recordings of these LVDTs were used to deduce the so-called sheet-pile wall 'head' displacement at the 'backfill surface level'.

Input excitations were applied at the base of the centrifuge models. The target input motions consisted of ramped sine waves with a dominant frequency of 1 Hz. The achieved input motions at the base

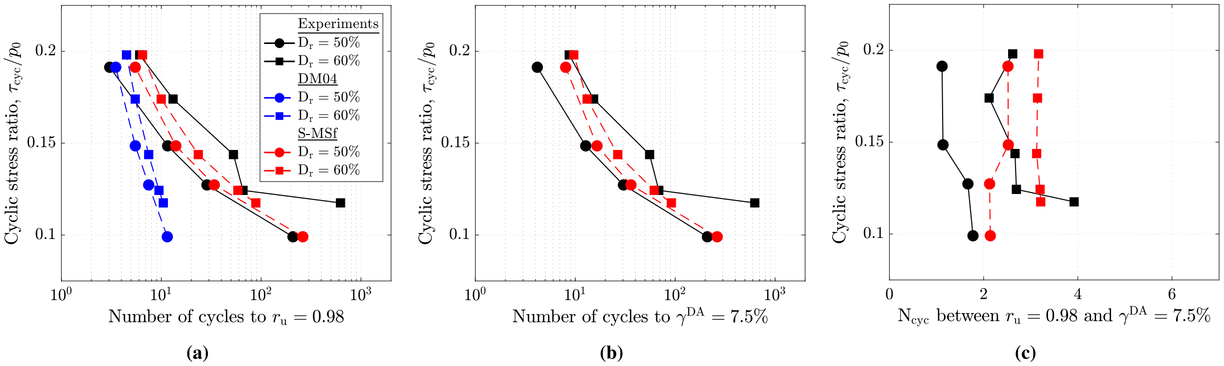

(a) (b) (c)

Fig. 5. Cyclic stress ratio vs. (a) number of cycles to reach $r_u = 0.98$, (b) number of cycles to reach $\gamma^{DA} = 7.5\%$, and (c) number of cycles between reaching $r_u = 0.98$ and $\gamma^{DA} = 7.5\%$, derived from undrained hollow cylinder cyclic torsional tests [7] and corresponding DM04 and S-MSf simulations on isotropically consolidated samples of Ottawa F65 sand with $D_r = 50\%$, 60%, and $p_0 = 100$ kPa.

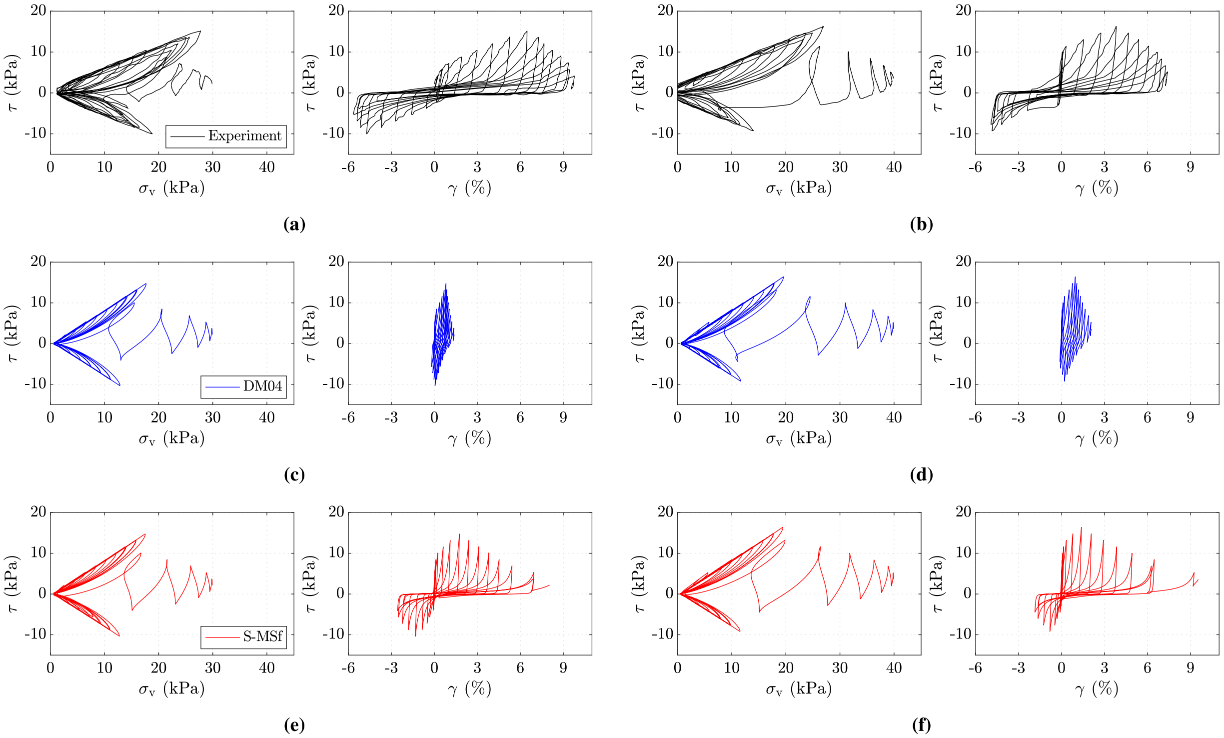

(a) (b) (c) (d) (e) (f)

Fig. 6. Stress path and stress–strain response from CDSS tests and corresponding simulations on K_0 consolidated samples of Ottawa F65 sand with non-zero static shear stress subjected to ramped sinusoidal motions: (a,b) experimental data from El Ghoraiby and Manzari [48] for $\sigma_{v0} = 30$, $\tau_{mean} = 2.6$ kPa, peak CSR = 0.42, and $\sigma_{v0} = 40$, $\tau_{mean} = 3.5$ kPa, and peak CSR = 0.31, respectively; (c-d) DM04 simulations, and (e-f) S-MSf simulations.

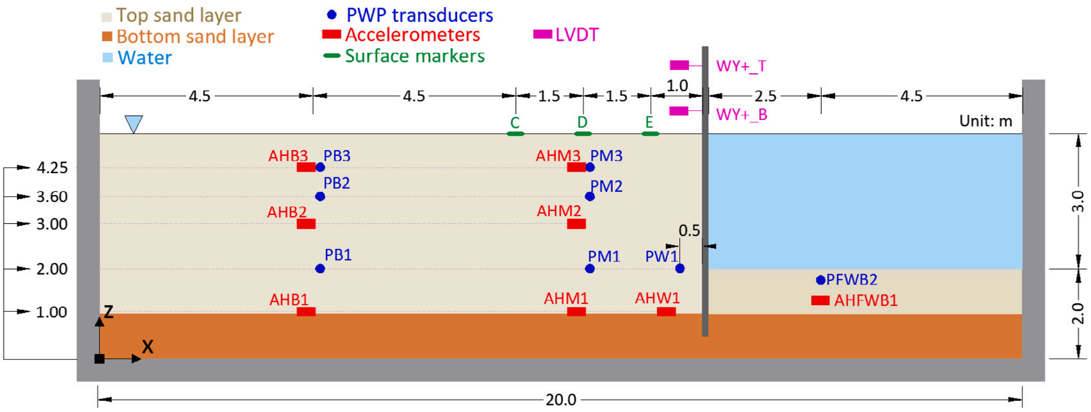

Fig. 7. Schematic setup of the target LEAP-2020 centrifuge tests, including the top and bottom submerged sand layers, sheet-pile wall, and the selected PWP transducers, accelerometers, surface markers, and displacement LVDTs.

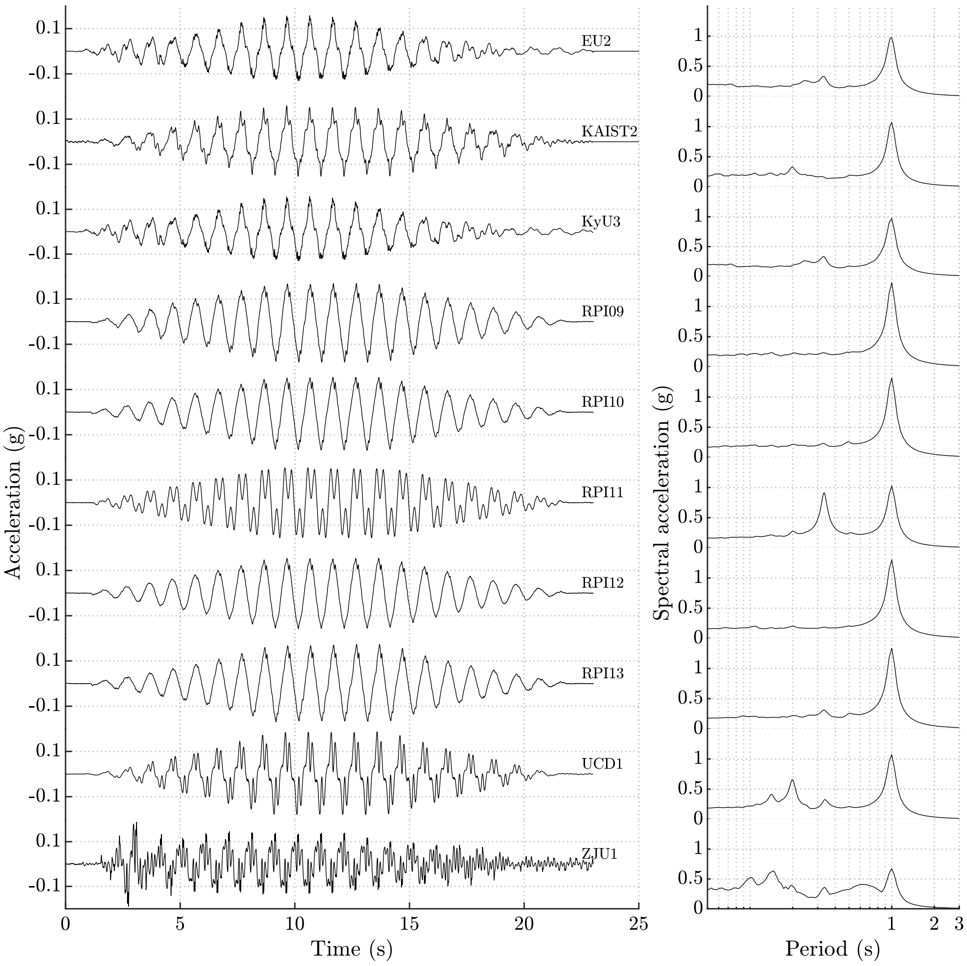

Fig. 8. Acceleration time histories and response spectra (5% damped) of the achieved base input motions in various centrifuge experiments.

Table 3
Main characteristics of the LEAP-2020 centrifuge tests.

Test ID	Centrif. accel. (g)	Top layer D_r (%)	Bottom layer D_r (%)	Sheet-pile thickness (m)	PGA (g)	CAV (m/s)
EU2	40	62.8	87.9	0.12	0.173	8.00
KAIST2	40	63.3	94.2	0.04	0.158	9.92
KyU3	40	64.7	64.7	0.12	0.158	8.03
RPI9	23	63.7	87.9	0.11	0.180	12.13
RPI10	23	65.9	91.3	0.11	0.169	11.19
RPI11	23	67.2	91.3	0.11	0.156	11.05
RPI12	23	56.0	91.3	0.11	0.158	11.22
RPI13	23	76.2	87.9	0.11	0.174	11.31
UCD1	27	70.8	93.2	0.11	0.187	9.56
ZJU1	26	74.0	74.0	0.10	0.190	8.67

of the centrifuge box in each test are presented in Fig. 8 in terms of acceleration time histories and the corresponding response spectra (5% damped). These motions show also higher frequencies because of both the intended design of target motions and the characteristics of the shaking system of the centrifuge facilities. The peak ground accelerations (PGA) and cumulative acceleration velocities (CAV) of the achieved input motions for all ten experiments are listed in Table 3.

3.2.2. Numerical model

The numerical model developed to simulate the LEAP-2020 centrifuge tests consisted of a 20.5 m long, 5.0 m high, and 1.0 m width in prototype scale. A total of 420 three-dimensional brick elements were used to build the full numerical model of the centrifuge setup, including a 1.0 m thick bottom sand layer, a 4.0 m thick top sand layer, and a 0.5 m thick sheet-pile modeled using solid elements, as shown in a two-dimensional view in Fig. 9. The spatial discretization in the x–z plane was at an equal size of 0.5×0.5 m in the soil domains in the back and front of the sheet-pile wall, and 0.25×0.5 m in the sheet-pile wall and the soil domain right underneath that. The zones had a thickness of 1.0 m in the y direction. Deformations along the y direction were fixed throughout the analysis, effectively rendering the model to behave in plane-strain conditions. This assumption was deemed reasonable, provided that lubricants were used to minimize the friction between the soil and the container in the centrifuge experiments. The sheet-pile wall was modeled using solid elements embedded into the ground, and the soil-wall contact was modeled using interface elements. The boundary conditions on the sides of the model were constrained laterally, while the base was fully fixed.

The soil layers in the model were initially modeled using a linear elastic material with a bulk modulus of 21.9×10^5 kPa and a shear modulus of 9.5×10^5 kPa, before switching to the S-MSf material model. The sheet-pile wall was modeled using a linear elastic material with a Young's modulus of 25.0×10^5 kPa and a Poisson's ratio of 0.31. These values were chosen to preserve the bending stiffness of the aluminum sheet-pile wall in the prototype scale, which has a Young's modulus of 69×10^6 kPa and a thickness of approximately 0.1 m. Coulomb frictional interface elements were placed along the sides and base of the wall to model the contact between the soil and structure, with shear and normal stiffnesses of 138.6×10^6 kPa and a friction angle of 20 degrees. The model was constructed sequentially, starting with dry layers of elastic material. Initially a flat deposit was created along the complete length of the model, resulting in the sheet-pile wall being fully

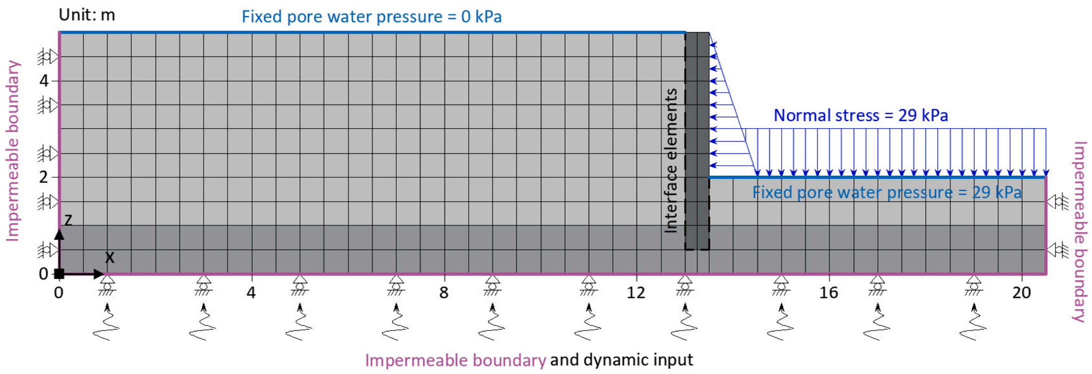

Fig. 9. Two-dimensional view of the centrifuge numerical model showing the spatial discretization and boundary conditions.

embedded around the soil elements. After bringing the dry model to equilibrium under 1 g gravity, the fluid-mechanical interaction module was activated. Here, an isotropic fluid model was used with a water bulk modulus of 2.0×10^5 kPa. The soil hydraulic conductivity was set to $k = 1.15 \times 10^{-4}$ kPa following the characterization reported in Kutter et al. [44]. The sheet-pile wall was considered impermeable by using a null fluid model. Pore water pressures at the upper boundary of the model were fixed at 0 kPa, and the system was brought to equilibrium again. After reaching equilibrium, the soil model was switched to S-MSf with the specified model constants in Table 2, and again the system was brought to mechanical and fluid equilibrium. The 3 m high excess top sand layer on the front side of the wall was then removed. This numerical approach to reproduce soil geometry was adopted for simplicity, and it differs from the procedure followed in the experiments in which, on the front side of the wall, no sand was placed above 2 m from the base of the model in the first place. Normal stress gradients representing the distribution of water pressure were applied to the right face of the wall and the soil surface on the front side of the sheet-pile, as illustrated in Fig. 9. Pore water pressures corresponding to submerged conditions were fixed for the grid points of the newly uncovered soil surface, resulting in the final configuration of the system. The model was once again brought to equilibrium. No provision was made for simulating the potential hydrodynamic effects of water on the front side of the sheet-pile wall. The same approach was used for the ten centrifuge models summarized in Table 3. Fig. 10 shows the contour plots of the initial state of stresses and pore water pressure for centrifuge model RPI9 before applying the achieved base motion. The pre-shaking states are considered reasonable, with an increase of pore water pressure from 0 kPa at the top to 50 kPa at the bottom of the model and zero pore pressure in the impermeable zones of the sheet-pile wall. Meanwhile, the initial lateral stress ratio σ_{xx}/σ_{zz} around the middle of the soil deposit ranged from 0.45 to 0.65. Finally, the dynamic module was activated and a Rayleigh damping of 1% with a central frequency of 2.5 Hz was adopted to reduce high-frequency numerical noise. The achieved input motions were then applied at the base of the model.

3.3. *Validation results*

The simulated response of the centrifuge model RPI9 was evaluated by comparing it to recorded experimental measurements in terms of acceleration, excess pore water pressure, and displacement time histories for the sensors depicted in Fig. 7. Fig. 11 illustrates the comparison of simulated and experimental time histories of acceleration. The simulations accurately capture the propagation of acceleration from the bottom to the top of the system until around 8 to 10 s. The subsequent occurrence of acceleration spikes, observed in both simulation and experiment, is often associated with sudden dilatancy and an increase of p, which upon reversal of loading leads to a sudden decrease of p. More specifically, in the simulations, after the Sf formulation degrades the plastic deviatoric stiffness at very low values of p, the dilatant response is accompanied by a strong recovery of plastic deviatoric stiffness, which is translated into the sharp acceleration spike, as shown in the simulation results. The corresponding acceleration response spectra for each sensor are presented in Fig. 12. The simulation accurately captures the spectral accelerations around the dominant period of 1 s. However, for periods smaller than 0.5 s, or frequencies higher than 2 Hz, the goodness-of-fit decreases, particularly for sensors that experienced strong dilatancy spikes around the wall. This discrepancy at higher frequencies is attributed to the underprediction of the simulated amplitude of the dilation spikes shown in Fig. 11. Despite this, the accurate prediction of the occurrence of dilation spikes, the satisfactory simulation of spectral accelerations for a relevant period range, and the reasonably well simulation of acceleration-time histories demonstrate the satisfactory predictive capabilities of the numerical modeling approach.

Fig. 13 illustrates the comparison of the time histories of excess pore water pressure from the simulations and experiments for the selected sensors. The comparisons show that the simulation is able to capture the increase of the excess pore pressure until the maximum values are attained, as indicated by the horizontal dashed lines, which occurred around 8 to 10 s across the system. However, the simulated response at sensors close to the wall, particularly sensors PM1, PM2, and PW1, shows a tendency for negative excess pore water pressures, i.e., an increase of p, following the 10-second mark, which is in contrast to the recorded response in the experiments. This response is likely influenced by the soil–structure interaction occurring around the sheet-pile wall and adjacent soil. Factors such as the adequacy of the representation of the initial state of stresses around the wall, the nature of the contact between the soil and sheet-pile wall, and the hydrodynamic effects of the water present in front of the wall may contribute to this discrepancy. Attempts to improve the simulation by using different approaches for generating the initial state of stress and different combinations of properties for the interface elements around the wall did not alleviate this discrepancy. Similar conclusions regarding these factors for simulating the excess pore water pressures around the wall were made in Basu et al. [55] for the same set of centrifuge experiments. It should be noted that the Coulomb-type interface model used for simulating the contact between soil and sheet-pile wall may not be appropriate for liquefaction-related problems, as these interfaces can be very sensitive to stiffness and normal stresses induced by the adjacent materials. In the case of liquefiable sand, the stiffness and normal stress can decrease very quickly. Assessing the suitability of these simple types of interfaces for liquefaction-related problems is beyond the scope of this study.

In Fig. 14, the simulated stress path and shear-stress strain response at the location of sensor PB1 are presented. The stress path exhibits a behavior that is more consistent with the CDSS tests from El Ghoraiby and Manzari [48] rather than the HCCTS tests by Vargas et al. [7] as discussed in Section 3.1. The response shows around 7 to 8 s of pre-liquefaction before experiencing a sudden decrease of p. The post-liquefaction response is characterized by large shear straining towards

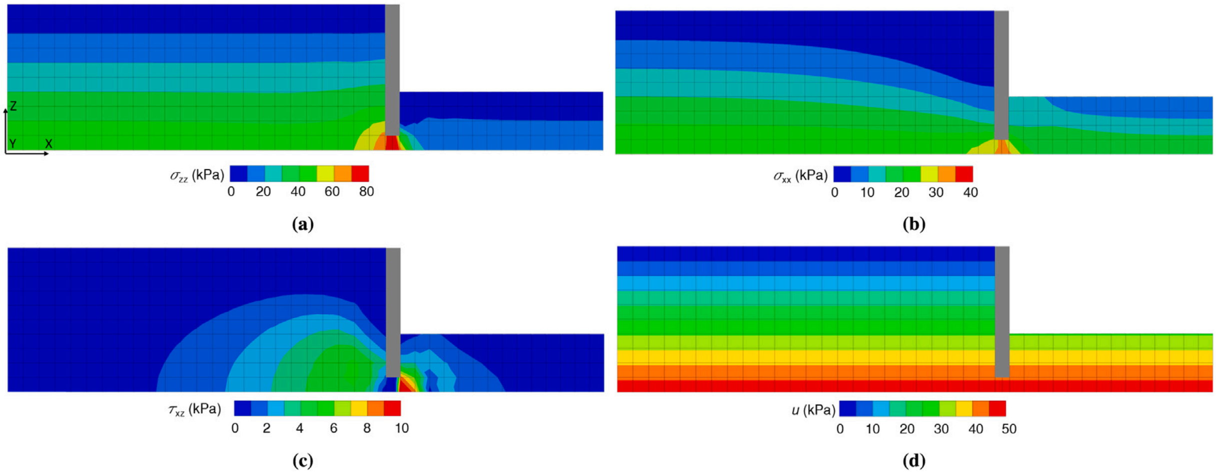

Fig. 10. Contours plots of the initial condition right before applying the base excitation in model RPkI9: (a) initial effective vertical stresses, (b) initial effective horizontal stresses, (c) initial shear stresses τ_{xz}, and (d) initial pore water pressures.

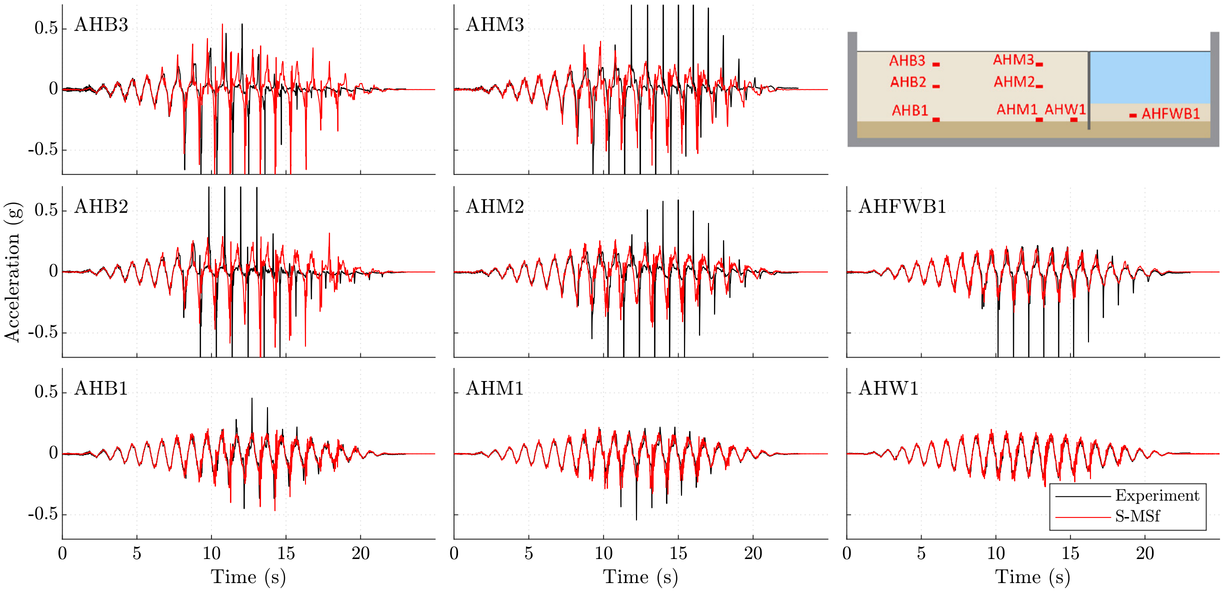

Fig. 11. Comparison of the simulated and measured acceleration time histories for the RPI9 test at various locations.

the direction of the wall displacement, as seen in the shear stress–strain plot. The pre-liquefaction stage is influenced by the memory surface (MS) in the constitutive model, as evidenced by the rapid growth of internal variable b^{M} prior to the onset of liquefaction. Upon reaching the dilatancy surface, the MS vanishes, resulting in much smaller values of b^{M} that do not affect the post-liquefaction response. Additionally, starting from 20 s and onward, the pore water pressure begins to dissipate, which causes the MS, and the value of b^{M}, to grow again. The accumulation of shear strain, primarily caused by the semifluidized state (Sf) formulation, is also evident in the time history of γ_{xz} at around 7 s. The history of internal variable ℓ reflects the progressive degradation of plastic deviatoric stiffness in the simulated response.

In the centrifuge experiment presented in this study, the primary engineering demand parameters of importance are the horizontal displacements and settlement of the soil deposit as well as the displacement of the sheet-pile wall at the end of shaking. Figs. 15 and 16 provide the histories of horizontal displacements and settlement, respectively, for several surface markers and the sheet-pile wall head. The simulated horizontal displacements for surface markers C, D, E, and for the sheet-pile wall head presented in Fig. 15 demonstrate a good prediction of the experimental response. The overall deformation of the soil–structure interaction system is well captured, particularly considering that the surface markers cover a distance of approximately 4.5 m behind the wall. This statement is further reinforced by the acceptable prediction of surface settlements shown in Fig. 16. Note that some phase differences between the experimental and simulated response are observed when it comes to the surface displacements of the system measured by high-speed cameras (e.g., see Fig. 15 for markers C, D, and E). Such phase differences can also be observed in other works stemming from LEAP centrifuge experiments [49,59,60]. In contrast, negligible or no phase difference is observed when evaluating the response measured using electronic transducers, such as accelerometers (see Fig. 11), pore pressure sensors (see Fig. 13), and LVDT (see Fig. 15 for the sheet-pile wall head). It is unclear whether the phase differences observed are caused by (a) the high-speed camera used for measurement or (b) a real mismatch between the simulated and experimental responses. Fig. 17 presents the end-of-shaking displacements for the centrifuge model RPI9, where the deformed mesh is magnified by a factor of 3, and the vectors represent the displacement magnitudes and directions. This figure shows that the shaking induced no noticeable curvature in the sheet-pile wall, but rather rotated it around its embedded portion at the base. Furthermore, it can be observed that most of the retained

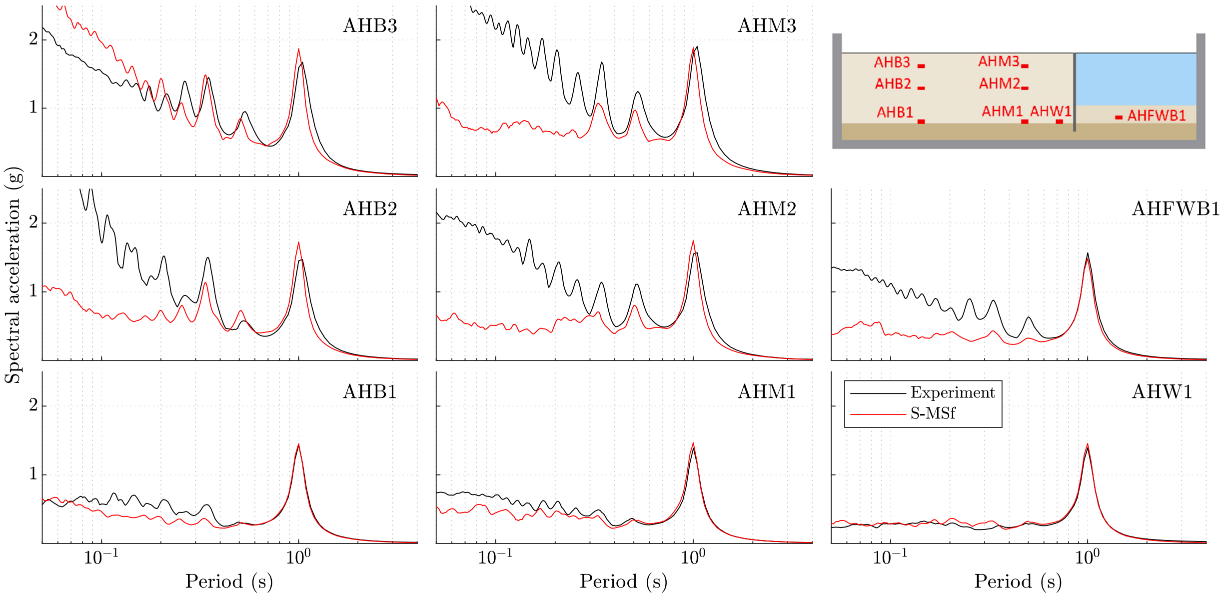

Fig. 12. Comparison of the simulated and measured acceleration response spectra (5% damped) for the RPI9 test at various locations.

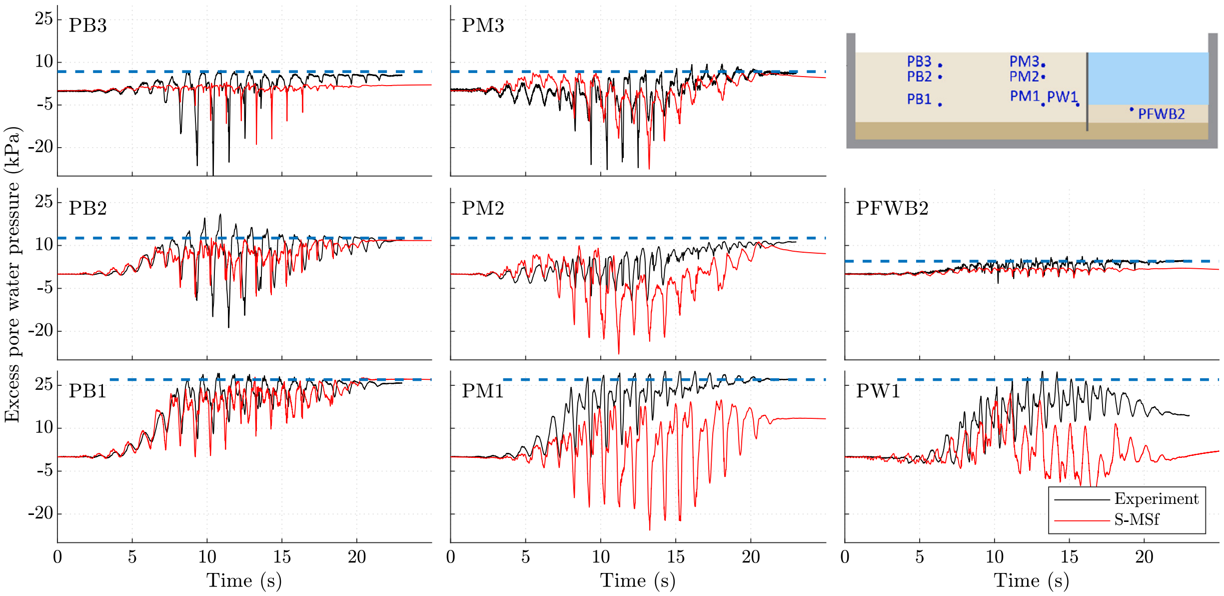

Fig. 13. Comparison of the simulated and measured excess pore water pressure for the RPI9 test at various locations. The dashed line indicates the initial vertical effective stress.

soil is subjected to translation towards the right of the system, while the portion closest to the sheet-pile wall experienced differential settlement with respect to its head. The figure also shows that the first 1.5–2 m of the soil surface in the front side of the wall bulges while the rest of the soil domain on the front of the wall experiences negligible permanent displacements.

The overall predictive capabilities for the complete dataset of centrifuge models are illustrated in Figs. 18 and 19 with respect to the end-of-shaking displacements. Fig. 18 summarizes the simulated and measured end-of-shaking horizontal displacements at surface markers D and E and at the sheet-pile wall head. These results indicate that the numerical modeling approach provides reasonable estimates of horizontal displacements for most centrifuge models, as they all lay within the line of 0.5:1 and 2:1. Fig. 19 presents a similar summary of surface settlements, with a slightly wider scatter in predicting the observed response those shown in Fig. 18. It is important to note that, due to the strong shaking and short-duration nature of the input motions in the LEAP-2020 experiments, all cases exhibited cyclic liquefaction after a few loading cycles and large deformations during most of the shaking duration. This implies that the response of the post-liquefaction stage had a greater impact than that of the pre-liquefaction stage. Recall that the two primary features of the S-MSf model, in comparison to the reference DM04 model, are the memory surface, which mainly operates in the pre-liquefaction stage, and the semifluidized state, which affects the response in the post-liquefaction stage. In light of this, it was observed that the semifluidized state of the S-MSf model was responsible for most of the reasonably accurate predictions seen earlier, while the memory surface ingredient played a lesser role due to the strong shaking nature of the motions.

4. Roles of pre- and post-liquefaction stages

In this section, the system response of liquefiable soil retained by a sheet-pile wall is examined through a sensitivity analysis. The validated

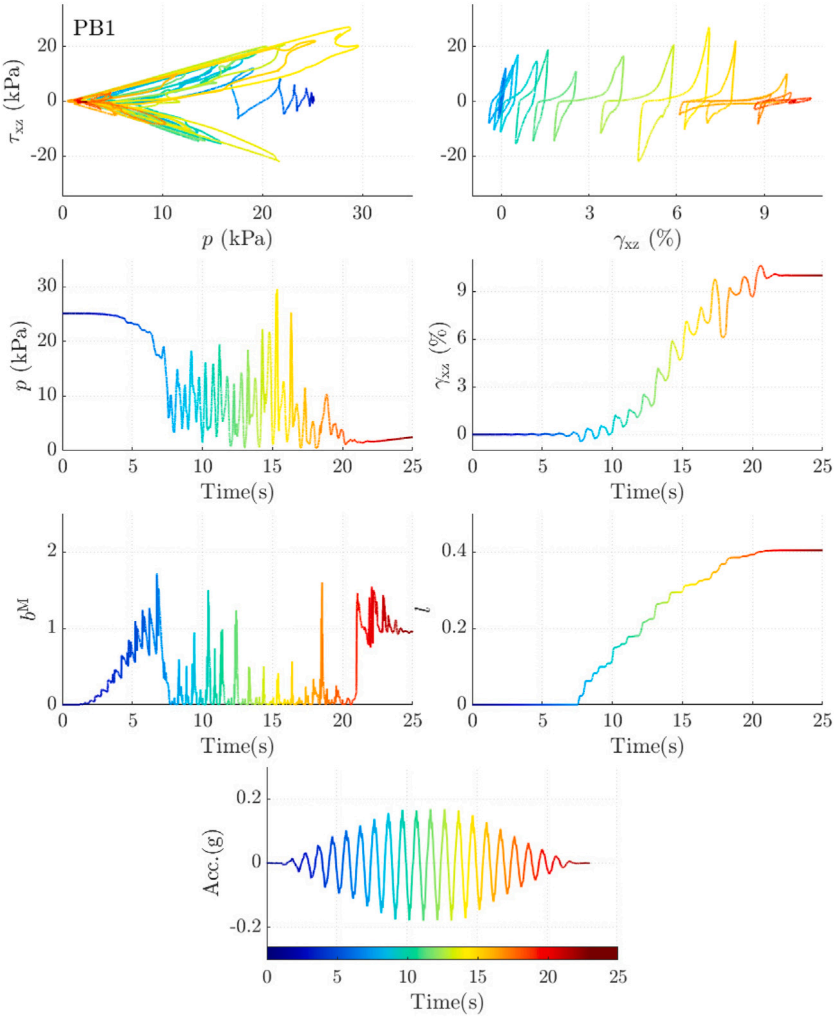

Fig. 14. Simulated stress path and stress–strain response at the location of sensor PB1 for the RPI9 test, and the corresponding time histories of mean pressure p, shear strain γ_{xz}, internal variables b^M and ℓ, and the base input motion.

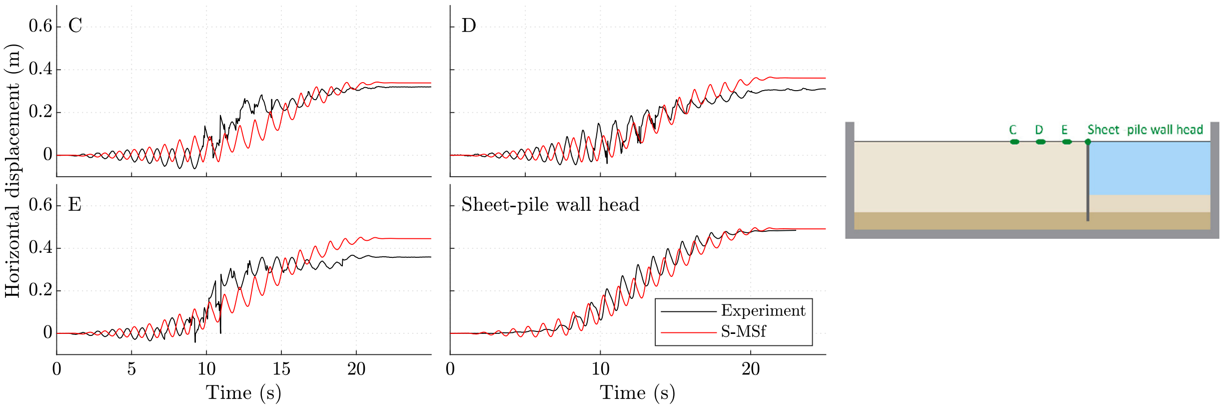

Fig. 15. Comparison of the simulated and measured surface horizontal displacements for the RPI9 test at various locations.

numerical model previously presented is utilized in simulations, in which a variety of base input motions are applied. These motions are designed to induce different degrees of liquefaction in terms of the extent of its occurrence throughout the soil deposit and the rate at which liquefaction is triggered. As a result of these simulations, a wide range of liquefaction-induced displacements of the soil and sheet-pile wall is observed. The strategy used in the sensitivity analysis and the results of the assessment, including the occurrence of cyclic liquefaction in the soil deposit, the effects on the dynamic response of the sheet-pile wall, and the overall system response, are described in detail.

4.1. Range of sensitivity analysis

The sensitivity analysis in this study is conducted using the numerical model previously used to simulate the centrifuge experiment

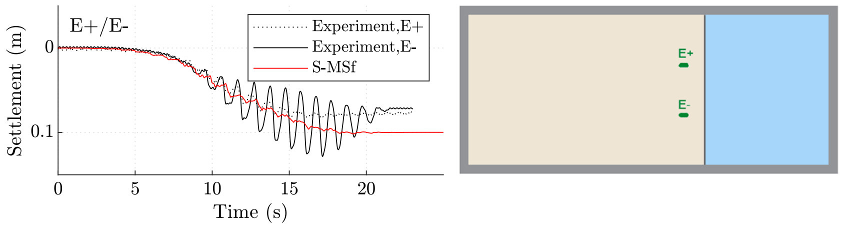

Fig. 16. Comparison of the simulated and measured surface settlements for the RPI9 test at various locations.

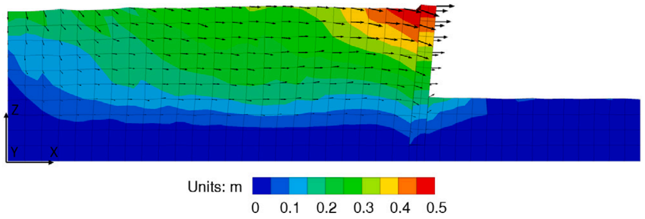

Fig. 17. Vectors and contours of simulated displacements at the end of shaking for RPI9. Mesh deformation is magnified by a factor of 3.

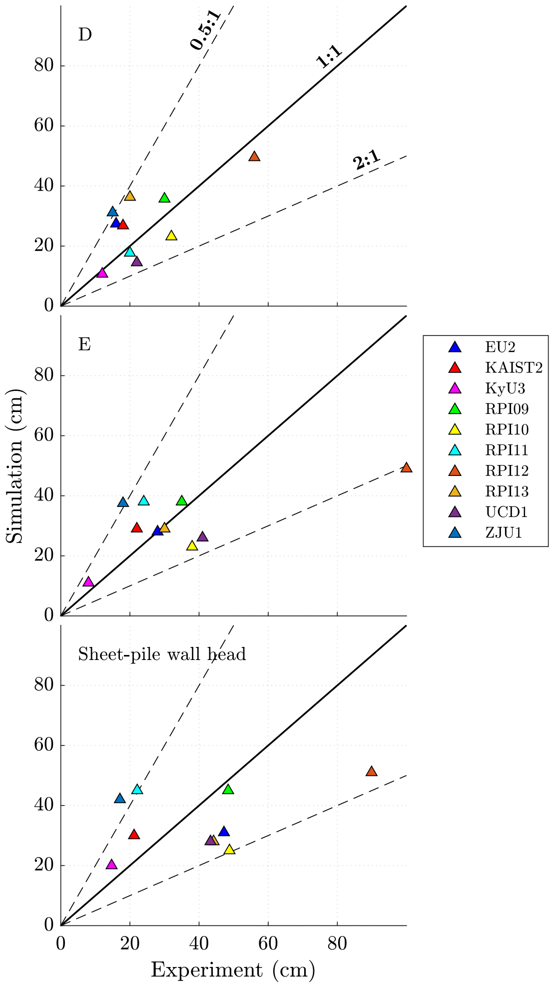

Fig. 18. Comparison of the simulated and measured end-of-shaking surface lateral displacements at various locations for all centrifuges tests.

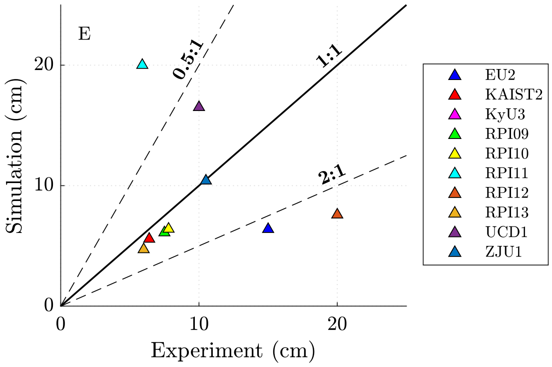

Fig. 19. Comparison of the simulated and measured end-of-shaking surface settlements at Marker 'E' for all centrifuges tests.

Table 4
Summary of the synthetic base input motions used for the sensitivity analysis.

Motion ID	Max. amplitude $\mathbf{a}_{\max}$ (g)	Duration $\mathbf{t}_{motion}$ (s)	CAV (m/s)
1	0.05	15	2.51
2	0.05	25	4.09
3	0.05	35	5.67
4	0.05	100	16.07
5	0.05	200	31.80
6	0.10	15	5.03
7	0.10	25	8.18
8	0.10	35	11.34
9	0.10	100	32.13
10	0.10	200	63.58
11	0.15	15	7.56
12	0.15	25	12.28
13	0.15	35	17.01
14	0.15	100	48.20
15	0.15	200	95.44

RPI9, which showed a satisfactory match between simulated and experimental results. The same model geometry and spatial discretization depicted in Fig. 9 is employed, and the S-MSf model is used with the model constants listed in Table 2. The sensitivity analysis is performed by using a wide range of base input motions with varying amplitudes and durations. The motions consist of synthetic ramped sinusoidal acceleration time histories with a fundamental frequency of 1 Hz, and small-amplitude frequencies of 0.4 and 0.1 Hz. The maximum amplitude ($a_{\max}$) and duration (t_{motion}) of the motions range from 0.05 to 0.15 g and from 15 to 200 s, respectively. The $a_{\max}$ is varied to evaluate the system response for a range of cyclic shear stress amplitudes, while different t_{motion} are used to study the system response under different numbers of loading cycles. Table 4 summarizes the 15 motions used for the sensitivity analysis, including their corresponding CAV values. Note that motions 14 and 15 have intensities much larger than those of actual earthquake records. Fig. 20 shows the acceleration times histories and response spectra of the base input motions with durations of 35 and 100 s. Note that the response spectra for synthetic motions with identical $a_{\max}$ but varied t_{motion} are fundamentally equal, suggesting that the use of intensity measures such as PGA or spectral acceleration is not sufficient to fully characterize the response of the system under investigation.

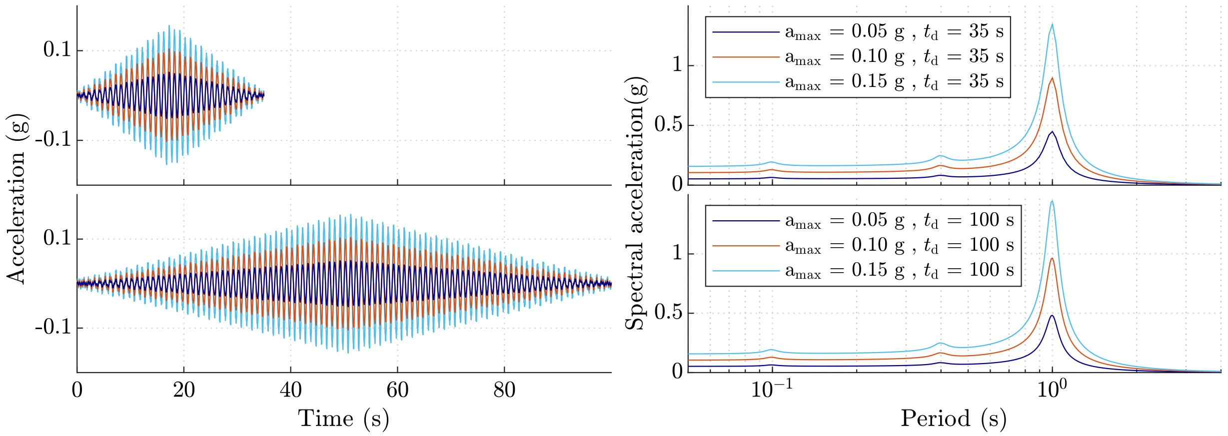

Fig. 20. Acceleration time histories and response spectra (5% damped) of base input motions used for the sensitivity analysis for maximum amplitudes a_{max} of 0.05, 0.10, and 0.15 g and durations t_{motion} of 35 and 100 s.

It is important to note that these synthetic motions were chosen over real earthquake ground motions to isolate the effects of shaking amplitude and duration with respect to frequency content and loading irregularity. By keeping the same spectral shape in all the motions, the potentially major impact of having different frequency contents for recordings of different t_{motion} is eliminated. Furthermore, it should be noted that the transient loading observed in real earthquake recordings is highly non-stationary, characterized by the alternation of accelerations with different amplitudes and frequencies in a seemingly random pattern, leading to isolated peaks that do not necessarily reflect the overall intensity of the acceleration record. This non-stationary behavior has been shown to have a significant impact on pore pressure development and liquefaction triggering, as demonstrated by laboratory experiments using irregular or earthquake-like loading patterns [61–63]. Therefore, the concept behind a_{max} in these synthetic motions should not be considered analogous to the typical concept of PGA used to characterize earthquake motions.

4.2. Occurrence of cyclic liquefaction

To evaluate the system response in the pre-liquefaction stage, the occurrence of cyclic liquefaction was analyzed using the results of the sensitivity analysis. Fig. 21(a) illustrates the time history of mean effective stress p at measurement location PB2 for a simulation subjected to a base input motion with $a_{max} = 0.10$ g and $t_{motion} = 35$ s. The liquefaction triggering time, depicted by vertical blue dashed lines, is defined as the first instance of p reaching a value less than 2 kPa, which occurred at approximately 14 s. This moment, referred to as t_{IL}, marks the boundary between the pre- and post-liquefaction stages at this measurement location. The significance of determining t_{IL} for assessing liquefaction triggering and its consequences are studied in recent works of Kramer et al. [64] and Ozener et al. [65] for site response analysis. Using t_{IL}, the acceleration time–history of the base input motion is also divided into two stages, as shown in Fig. 21(b). Similar assessments are presented in Fig. 21(c) and 21(d) for the time-histories of base input CAV and horizontal displacements of the sheet-pile wall head, respectively, which will be discussed in more detail later.

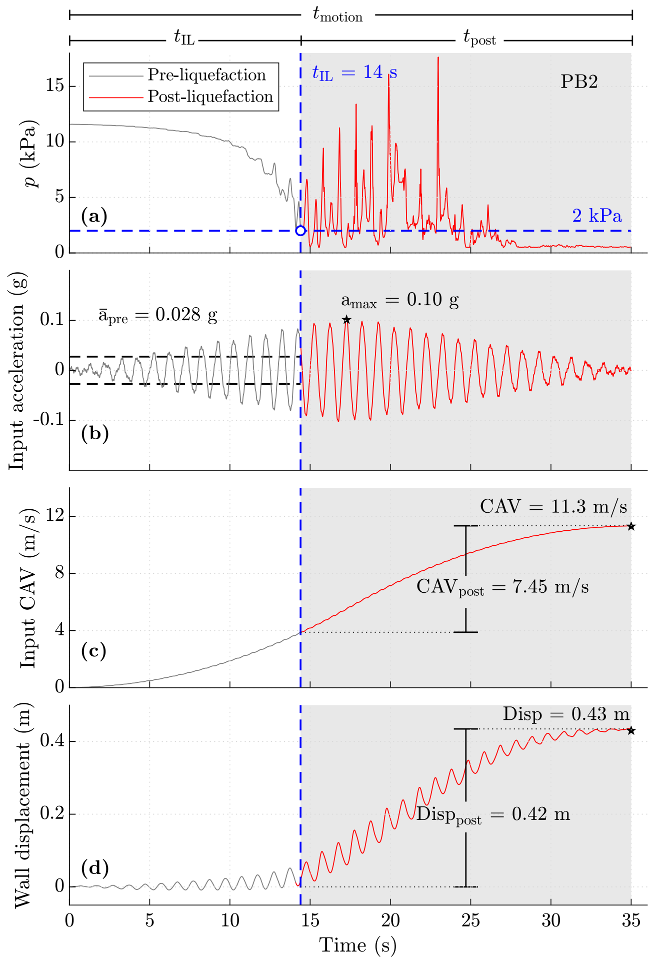

Fig. 21. Time histories of (a) mean effective stresses p at measurement location PB2, (b) base input acceleration, (c) base input CAV, and (d) horizontal displacements of sheet-pile wall head, for the simulation with motion ID 8. The t_{IL} is determined for PB2 and used to derive the corresponding $\bar{a}_{pre}$, CAV_{post}, and $Disp_{post}$.

To characterize the portion of a base excitation that leads to liquefaction triggering at a measurement location, a new intensity measure, $\bar{a}_{pre}$, is defined by averaging the absolute values of accelerations until t_{IL}. This measure represents the amplitude of equivalent uniform loading cycles in the pre-liquefaction stage and is similar to the concept used in simplified liquefaction triggering procedures such as that proposed by Idriss and Boulanger [10] to characterize the overall seismic demand. Using this measure, $\bar{a}_{pre} = 0.028$ g was determined for $t_{IL} = 14$ s at measurement location PB2 as shown in Figs. 21(a,b). Following the above procedure, for any location in the soil deposit that experienced cyclic liquefaction, the corresponding pairs of t_{IL} and $\bar{a}_{pre}$ can be determined. In the system analyzed in this work, measurement locations PB2, PB3, PM2, and PM3 were considered to be representative of the liquefaction response as the triggering of liquefaction around

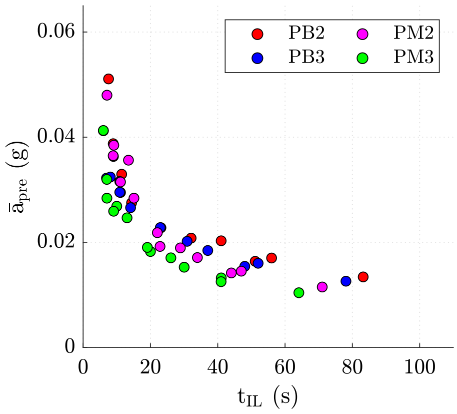

Fig. 22. The amplitude of equivalent uniform loading cycles in pre-liquefaction, $\bar{a}_{pre}$, against the timing of initial liquefaction, t_{IL}, for measurement locations PB2, PB3, PM2, and PM3.

these locations heavily influenced the seismic displacements of the soil deposit and sheet-pile wall head. To summarize the pre-liquefaction response for all the analyses, Fig. 22 shows the pairs of t_{IL} and $\bar{a}_{pre}$ for these measurement locations with respect to the base input motion. Cases that did not experience cyclic liquefaction are not included in this illustration. The results indicate that relatively large values of $\bar{a}_{pre}$ between 0.03 and 0.05 g trigger cyclic liquefaction in less than 20 s. On the other hand, for values of $\bar{a}_{pre}$ lower than 0.02 g, liquefaction triggering takes a longer time, in the range of 20–80 s.

The relationship between t_{IL} and $\bar{a}_{pre}$ presented in Fig. 22 is similar to those of typical cyclic resistance curves, such as Fig. 5(b). The horizontal axes of these figures are related to a measure of soil resistance to liquefaction (number of cycles or time) and their vertical axes are associated with a measure of demand exerted by cyclic loading (CSR or acceleration amplitude). In this sense, using $\bar{a}_{pre}$ paired with t_{IL} appears to capture the triggering response of the system for the complete range of acceleration amplitudes, 0.05 to 0.15 g, and durations, 15 to 200 s, of the base input motion. The results presented here indicate that the pre-liquefaction stage plays an important role in defining t_{IL} which is closely related to the cyclic resistance of the soil and the intensity of shaking, here characterized by $\bar{a}_{pre}$. The role of t_{IL} is significant as it defines how much of the remaining shaking duration is spent in post-liquefaction, that is the stage responsible for the majority of the liquefaction-induced displacements, as it is detailed later in the paper.

To achieve a reliable simulation of the occurrence of cyclic liquefaction at the system level, it is essential to have an accurate simulation of the pre-liquefaction response of soil at the element-level. To achieve this, a detailed laboratory program that includes cyclic tests covering a wide range of CSR values is required. These tests should be used to calibrate the constitutive model constants, which should accurately capture the stress path response and the number of cycles to liquefaction. It is important to note that the lower end of the CSR values in cyclic resistance curves should not be overlooked, as performance-based design practice often requires determining the seismic response of geostructures for a variety of ground motions determined from probabilistic seismic hazard studies, each one with a range of amplitudes and frequency content [1]. For example, in the case of hazard analysis of dams, these studies quantify the seismic hazard for a range of return periods, which include those associated with short-term and long-term scenarios, i.e., operational and closure conditions, respectively, as specified by regulatory agencies such as the Canadian Dam Association [66]. It is also important to note that the choice of solid-fluid interaction model constants, such as hydraulic conductivity, can also have a major impact on the resulting development of excess pore water pressures and, consequently, t_{IL}. A thorough analysis would likely need to consider the potential changes of permeability before, during, and after liquefaction [67,68], or use a simplified approach such as considering an increased hydraulic conductivity throughout the analysis [35]. The current study has not accounted for these considerations.

4.3. Cyclic liquefaction consequences

In soil–structure interaction problems involving soil liquefaction, such as those related to shallow foundations [69,70], deep pile foundations [71,72], or underground structures [73,74], the quantification of the consequences of cyclic liquefaction is often done through the measurement of liquefaction-induced displacements, which primarily develop at the post-liquefaction stage. In this section, the post-liquefaction response is evaluated by measuring horizontal displacements at the top of the sheet-pile wall. Based on the understanding that the majority of accumulated displacements occur during the post-liquefaction stage of response, the pre- and post-liquefaction timing for the selected measurement locations are determined following the approach presented in Fig. 21(a) for PB2. Here, t_{post} is determined by subtracting t_{IL} from t_{motion}, and $\bar{a}_{post}$ is calculated in a similar manner as $\bar{a}_{pre}$ but for t_{post}. Additionally, CAV_{post} is identified as the portion of base motion CAV that corresponds to t_{post}, as shown in Fig. 21(c). Finally, $Disp_{post}$ is calculated through the use of the history of wall displacements in a similar manner as shown in Fig. 21(d). It should be noted that the use of post-liquefaction terminology per measurement location to describe the wall response may not be entirely accurate as the system response of the entire soil body and the wall influences the wall displacements. However, for the purposes of this study, this simplification is considered acceptable as the t_{IL} values determined from the selected measurement locations provide reasonable estimates of the time at which wall head displacements start to accumulate significantly, as illustrated in Fig. 21(d) where the majority of the displacements occur after t_{IL} = 14 s.

Fig. 23 presents the sensitivity analysis results for $Disp_{post}$ against the corresponding $\bar{a}_{post}$ and t_{post} for four measurement locations in the backfill. The results clearly show that using either $\bar{a}_{post}$ or t_{post} alone would not be sufficient to estimate $Disp_{post}$. In fact, Fig. 23(a) reveals that for approximately the same value of $\bar{a}_{post}$, the obtained displacements in the post-liquefaction stage can be significantly different, depending on the value of t_{motion}, with the longer motions resulting in larger displacements. Similar observation can be made in Fig. 23(b) with respect to t_{post}, with larger values of $Disp_{post}$ for higher a_{max}. To take into account the combined effects of acceleration amplitude and duration in the post-liquefaction stage, the CAV_{post} is used and presented in Fig. 24 against the obtained $Disp_{post}$ for the measurement locations in all 15 sensitivity analyses. The results demonstrate that CAV_{post} obtained at several locations in the soil deposit adequately characterizes the post-liquefaction response in terms of deformations. This finding is consistent with those of previous works on the efficiency of evolutionary intensity measures, such as CAV, for predicting liquefaction-induced damage [70,75,76]. The assessment of the soil response in the post-liquefaction stage reveals that its role is to control the magnitude of the liquefaction-induced displacements, which is in turn defined not only by the soil's potential to develop large cyclic shear strains but also by the CAV_{post} that evolves after t_{IL}.

In order to simulate the effects of cyclic liquefaction accurately, it is crucial to have a numerical modeling approach that, at the element-level, can replicate the development of cyclic shear strains during the post-liquefaction stage. To achieve this, the corresponding laboratory testing program used for the model calibration should include cyclic tests with shear strain accumulation in the post-liquefaction stage. It is worth noting that the pattern of cyclic strain accumulation can vary depending on the initial stress and loading conditions. This has been demonstrated in studies by Vargas et al. [7] and El Ghoraiby and Manzari [48], where the presence or absence of static shear stress affected the symmetry and accumulation of the resulting cyclic shear strains in post-liquefaction. Therefore, it is essential that the initial

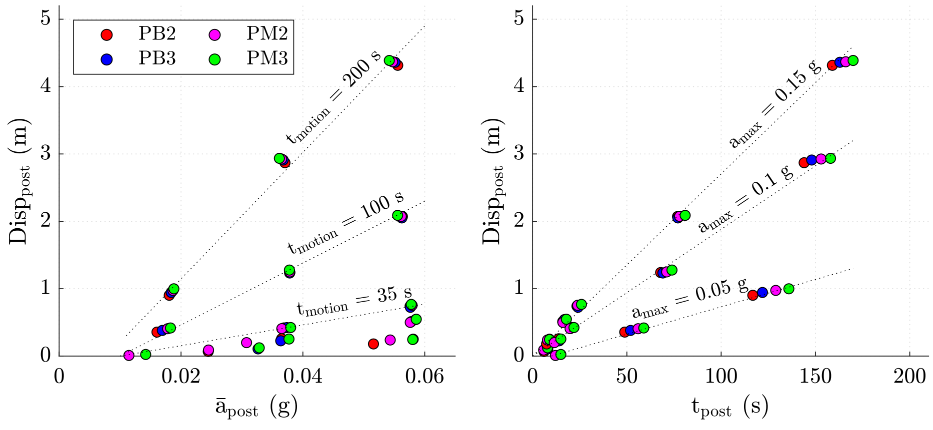

(a) **(b)**

Fig. 23. Horizontal displacements of sheet-pile wall head occurred during post-liquefaction, $Disp_{post}$, against (a) amplitude of the equivalent uniform loading cycles in post-liquefaction, $\bar{a}_{post}$, and (b) duration of shaking in post-liquefaction, t_{post}. Results are shown for measurement locations PB2, PB3, PM2, and PM3.

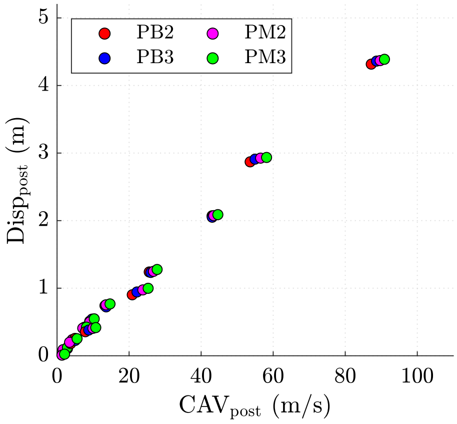

Fig. 24. Horizontal displacements of sheet-pile wall head occurred during post-liquefaction, $Disp_{post}$, against the base input motion CAV_{post} in post-liquefaction for measurement locations PB2, PB3, PM2, and PM3.

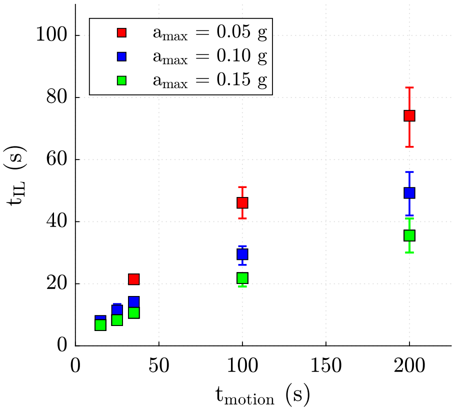

Fig. 25. Effects of motion duration t_{motion} and maximum acceleration amplitude a_{max} on the average and variation of timing of initial liquefaction t_{IL} at selected measurement locations.

and shearing conditions in the laboratory tests closely resemble the expected conditions of the system being evaluated. The deformation patterns and magnitudes observed in these tests should then be used to guide the calibration of model constants related to the post-liquefaction response.

4.4. Assessment of system response

The observations obtained in the preceding relied on dividing the response of soil into pre- and post-liquefaction stages based on element-scale quantification of cyclic liquefaction triggering and other related quantities. This section presents an assessment of the overall system response. To evaluate the impact of the pre-liquefaction stage on the overall system response, the average and variation of timing initial liquefaction at selected measurement locations (PB2, PB3, PM2, and PM3) were obtained for all ground motions. The results, presented in Fig. 25, indicate that for a given maximum acceleration a_{max}, the amount of time the system experiences in the pre-liquefaction stage t_{IL} increases with the duration of the ground motion t_{motion}. Additionally, the results show that for a given duration of ground motion, t_{IL} decreases with increasing maximum acceleration. These observations reveal that for the functional form of the ground motions selected in this sensitivity analysis, the largest values of t_{IL} correspond to those ground motions with long durations and small amplitude accelerations.

To assess the impact of the post-liquefaction stage, in which most of the system's seismic displacements occur, the end-of-shaking horizontal displacements of the sheet-pile wall head and the soil surface settlement at the surface measurement point E are presented in Fig. 26. Both displacements increase with t_{motion} and a_{max}, as depicted in Figs. 26(a,c). Figs. 26(b,d) present the same system displacements with respect to the CAV of the base input motions. As was discussed earlier for Fig. 24, this evolutionary intensity measure appropriately characterizes the shaking with respect to liquefaction-induced displacements.

In summary, the primary role of the pre-liquefaction stage in the system response is to control the extent and timing of liquefaction triggering, which varies with respect to the intensity of the base input motion, as shown in Fig. 25. The timing of liquefaction triggering is a critical factor as it dictates the duration of the remaining shaking, which is responsible for most of the permanent displacements in the system. Once liquefaction has occurred, the post-liquefaction stage plays a key role in controlling the magnitude of the permanent displacements based on the soil's potential for accumulating large cyclic strains. These roles are exemplified in Figs. 25 and 26(b,d), with the former showing that for the same duration, the t_{IL} decreases with increasing a_{max}, while the latter showing the corresponding displacements increase because more time is allotted to develop large deformations.

These observations suggest that the first requirement of a numerical modeling framework for adequate prediction of liquefaction-induced displacements is the accurate simulation of the extent and timing of

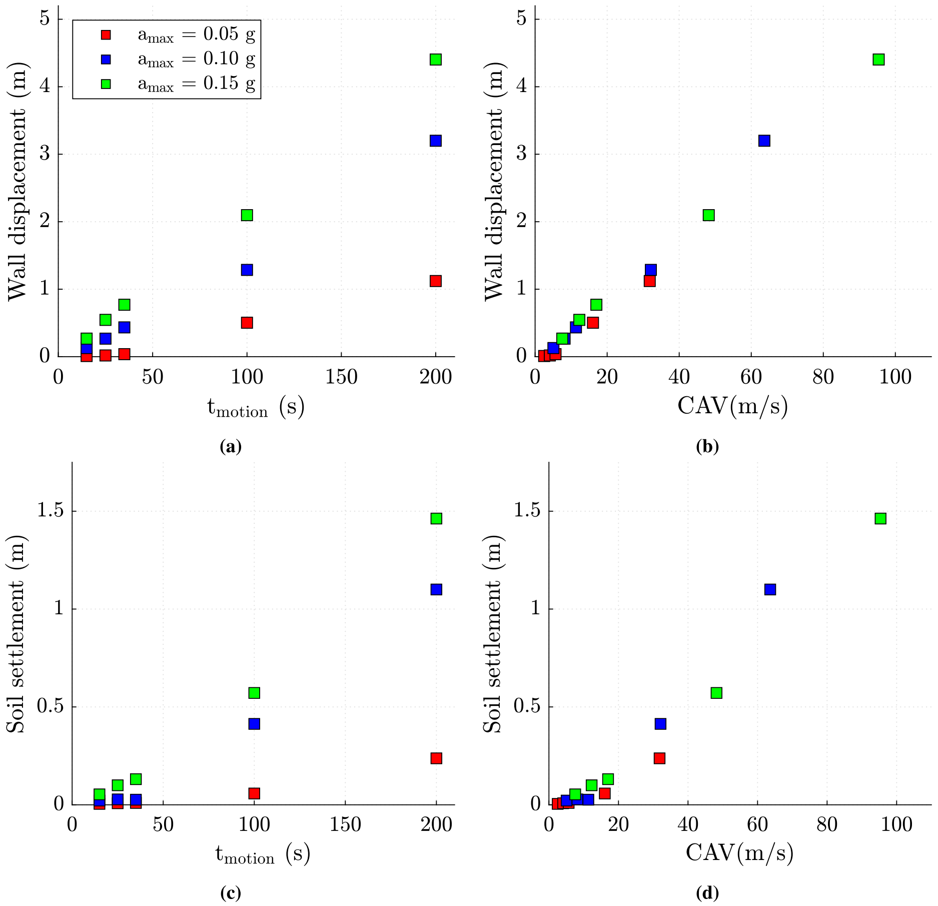

(a) (b)

(c) (d)

Fig. 26. Effects of the motion characteristics, including duration t_{motion}, maximum acceleration amplitude a_{max}, and CAV, on the end-of-shaking horizontal displacement of wall head and soil surface settlement at the surface measurement point E.

the occurrence of cyclic liquefaction. Inadequate assessment of the response in the pre-liquefaction stage results in inaccurate quantification of the ensuing system displacements, regardless of the capability of the modeling approach in simulating the post-liquefaction deformations. Similarly, a numerical modeling approach's ability to simulate liquefaction triggering does not guarantee reliable estimations of the system's liquefaction-induced displacements. The highlight of the constitutive modeling framework of the S-MSf model is its ability to capture the responses in both pre- and post-liquefaction stages adequately, using the same model constants and without one affecting the reliability of the other.

5. Summary and conclusions

The objective of this study was to thoroughly examine the impact of liquefaction on the seismic response of sand supported by a sheet-pile wall, with a particular emphasis on the influence of both the pre- and post-liquefaction stages. The newly formulated SANISAND-MSf constitutive model is used for this purpose, which has been developed to accurately model the progressive reduction of mean effective stress that occurs during pre-liquefaction and the evolution of substantial cyclic shear strains during post-liquefaction under cyclic shearing conditions. The model achieves this through the use of a memory surface, which enhances and better controls the plastic stiffness in the pre-liquefaction stage, and the concept of a semifluidized state and a related internal variable, which degrades the plastic deviatoric stiffness during the post-liquefaction stage.

The model simulative accuracy was first validated using a series of centrifuge tests conducted as part of the LEAP-2020 project, which consisted of submerged sand deposits supported by a sheet-pile wall subjected to dynamic excitations at the base. The model constants were determined from cyclic hollow cylinder torsional shear tests and cyclic direct simple shear tests, all with initial states and stresses resembling those experienced by soil in the centrifuge tests, including those with non-zero mean shear stress. The validation results based on the centrifuge tests demonstrate the capability of the newly formulated S-MSf model and the overall numerical modeling approach to accurately depict the dynamic response of the liquefiable sand-sheet-pile wall system. The simulations were able to replicate the acceleration time–history, capturing the observed dilation-induced pulses that occur after cyclic liquefaction is triggered. The simulations also captured the evolution of excess pore water pressure within the soil deposit. Moreover, the end-of-shaking displacements, both vertical and horizontal, of the soil and the sheet-pile wall were well captured by the simulations, providing a strong validation of the model's ability to accurately simulate the seismic response of this type of system.

The roles of pre- and post-liquefaction responses were studied by conducting a sensitivity analysis where two contributors were changed: (a) the duration of the base input motion was varied from 15 to 200 s, and (b) the maximum acceleration amplitude of the base input motion was varied from 0.05 to 0.15 g. These combinations produced 15 base input motions covering a wide range of cumulative absolute velocities. This analysis revealed that the seismic demand imposed by the base input motion needs to be characterized in terms of stage-specific intensity measures in order to evaluate the roles of pre- and post-liquefaction stages. The response in pre-liquefaction can be described using a pair of intensity measures associated with the acceleration amplitude of equivalent uniform loading cycles in pre-liquefaction and the corresponding time to trigger cyclic liquefaction. On the other hand, the permanent displacements accumulating during the post-liquefaction stage can be characterized by the cumulative absolute velocity that evolves after liquefaction triggering. The results from the sensitivity analysis showed that the major role of the response in the pre-liquefaction stage is to control the timing and extent of the occurrence of cyclic liquefaction throughout the soil deposit. This is critical as it defines how much of the remaining shaking is spent in post-liquefaction. The role of the post-liquefaction stage resides in its potential to develop large cyclic strains, which along with the time allotted by the response in the pre-liquefaction stage, determines the magnitude of the permanent displacements of the system.

The memory surface ingredient of the S-MSf model was crucial in accurately modeling the occurrence and timing of cyclic liquefaction, while the semifluidized state largely controlled the magnitude of liquefaction-induced displacements. The results of the sensitivity analysis emphasized the importance of considering the roles of both pre- and post-liquefaction stages in the evaluation of the seismic response of liquefiable sand supported by a sheet-pile wall. Accurately modeling the response in both stages is essential for a reliable prediction of the system's response. The study highlights the potential of the S-MSf constitutive model to achieve this goal, and provides valuable insights for future research in this area.

CRediT authorship contribution statement

Keith Perez: Conceptualization, Methodology, Software, Validation, Formal analysis, Data curation, Writing – original draft, Visualization. **Andrés Reyes:** Conceptualization, Methodology, Software, Validation, Formal analysis, Data curation, Writing – original draft, Visualization. **Mahdi Taiebat:** Conceptualization, Methodology, Validation, Resources, Writing – review & editing, Supervision, Project administration, Funding acquisition.

Declaration of competing interest

The authors declare that they have no known competing financial interests or personal relationships that could have appeared to influence the work reported in this paper.

Acknowledgments

Financial support for this study was provided by the Natural Sciences and Engineering Research Council of Canada (NSERC). The authors would like to thank the organizers and participants of LEAP for stimulating discussions over the last few years. The authors are also grateful to Dr. Trevor Carey for the discussions and valuable review comments and to Dr. Gabriele Chiaro for sharing the undrained cyclic test data on Toyoura sand.

References

[1] Kramer SL, Mitchell RA. Ground motion intensity measures for liquefaction hazard evaluation. Earthq Spectra 2006;22(2):413–38.

[2] Hayashi S, Kubo K, Nakase A. Damage to harbour structures by the Niigata earthquake. Soils Found 1966;6(1):89–112.

[3] Ishihara K, Yoshida K, Kato M. Characteristics of lateral spreading in liquefied deposits during the 1995 Hanshin-Awaji earthquake. J Earthq Eng 1997;1(1):23–55.

[4] Motamed R, Towhata I, Honda T, Yasuda S, Tabata K, Nakazawa H. Behaviour of pile group behind a sheet pile quay wall subjected to liquefaction induced large ground deformation observed in shaking test in E-defense project. Soils Found 2009;49(3):459–75.

[5] Madabhushi SPG, Saito K, Booth ED. EEFIT mission to Haiti following the 12th january 2010 earthquake. Bull Earthq Eng 2013;11:35–68.

[6] Wichtmann T, Triantafyllidis T. An experimental database for the development, calibration and verification of constitutive models for sand with focus to cyclic loading: part I—tests with monotonic loading and stress cycles. Acta Geotech 2016;11(4):739–61.

[7] Vargas RR, Ueda K, Uemura K. Influence of the relative density and K_0 effects in the cyclic response of Ottawa F-65 sand - cyclic Torsional Hollow-Cylinder shear tests for LEAP-ASIA-2019. Soil Dyn Earthq Eng 2020;133:106111.

[8] Ishihara K. Liquefaction and flow failure during earthquakes. Géotechnique 1993;43(3):351–415.

[9] Youd TL, Idriss IM, Andrus RD, Arango I, Castro G, Christian JT, et al. Liquefaction resistance of soils: Summary report from the 1996 NCEER and 1998 NCEER/NSF workshops on evaluation of liquefaction resistance of soils. J Geotech Geoenviron Eng 2001;127(10):817–33.

[10] Idriss IM, Boulanger RW. Soil liquefaction during earthquakes. Earthquake Engineering Research Institute; 2008.

[11] Yang M, Taiebat M, Radjaï F. Liquefaction of granular materials in constant-volume cyclic shearing: Transition between solid-like and fluid-like states. Comput Geotech 2022;148:104800. http://dx.doi.org/10.1016/j.compgeo.2022.104800.

[12] Umar M, Chiaro G, Kiyota T, Ullah N. Deformation and cyclic resistance of sand in large-strain undrained torsional shear tests with initial static shear stress. Soils Found 2021;61(3):765–81.

[13] Iai S, Matsunada Y, Kameoka T. Strain space plasticity model for cyclic mobility. Soils Found 1992;32(2):1–15.

[14] Iai S, Ueda K, Tobita T, Ozutsumi O. Dilatancy of granular materials in a strain space multiplemechanism model. Int J Numer Anal Methods Geomech 2013;35:360–92.

[15] Prevost JH. A simple plasticity theory for frictional cohesionless soils. Soil Dyn Earthq Eng 1985;4(1):9–17.

[16] Khosravifar A, Elgamal A, Lu J, Li J. A 3D model for earthquake-induced liquefaction triggering and post-liquefaction response. Soil Dyn Earthq Eng 2018;110:43–52.

[17] Elgamal A, Yang Z, Parra E, Ragheb A. Modeling of cyclic mobility in saturated cohesionless soils. Int J Plast 2003;19(6):883–905.

[18] Dafalias YF. Bounding surface plasticity. I: Mathematical foundation and hypoplasticity. J Eng Mech 1986;112(9):966–87.

[19] Boulanger RW, Ziotopoulou K. PM4sand (version 3.1): A sand plasticity model for earthquake engineering problems. Tech. Rep. UCD/CGM-17/01, Center for Geotechnical Modeling, Department of Civil and Environmental Engineering, University of California, Davis; 2017.

[20] Cheng Z, Detournay C. Formulation, validation and application of a practice-oriented two-surface plasticity sand model. Comput Geotech 2021;132:103984.

[21] Dafalias YF, Manzari MT. Simple plasticity sand model accounting for fabric change effects. J Eng Mech 2004;130(6):622–34.

[22] Wang R, Cao W, Xue L, Zhang J. An anisotropic plasticity model incorporating fabric evolution for monotonic and cyclic behavior of sand. Acta Geotech 2021;16(1):43–65.

[23] Yu J, Wang R, Zhang J-M. Importance of liquefaction resistance and fabric anisotropy simulation capability of constitutive models for liquefiable seismic response analysis. Comput Geotech 2022;150:104928.

[24] Wang R, Zhang J-M, Wang G. A unified plasticity model for large post-liquefaction shear deformation of sand. Comput Geotech 2014;59:54–66.

[25] Yang M, Taiebat M, Dafalias YF. SANISAND-MSf: a sand plasticity model with memory surface and semifluidised state. Géotechnique 2022;72(3):227–46.

[26] Iai S, Kameoka T. Finite element analysis of earthquake induced damage to anchored sheet pile quay walls. Soils Found 1993;33(1):71–91.

[27] Iai S. Evaluation of performance of port structures during earthquakes. Soil Dyn Earthq Eng 2019;126:105192.

[28] Manzari MT, Kutter BL, Zeghal M, Iai S, Tobita T, Madabhushi SPG, et al. LEAP projects: concept and challenges. In: Iai S, editor. Geotechnics for catastrophic flooding events. Taylor & Francis Group London; 2015, p. 109–16.

[29] Itasca. FLAC3D: Fast Lagrangian analysis of continua in three-dimensions, version 7.0. Minneapolis, Minnesota, USA: Itasca Consulting Group, Inc.; 2019.

[30] Barrero AR. Multi-scale modeling of the response of granular soils under cyclic shearing (Ph.D. thesis), Vancouver, BC, Canada: Department of Civil Engineering, University of British Columbia; 2019.

[31] Taiebat M, Dafalias YF. SANISAND: Simple anisotropic sand plasticity model. Int J Numer Anal Methods Geomech 2008;32(8):915–48.

[32] Taiebat M, Jeremić B, Dafalias YF, Kaynia AM, Cheng Z. Propagation of seismic waves through liquefied soils. Soil Dyn Earthq Eng 2010;30(4):236–57.

[33] Ramirez J, Barrero AR, Chen L, Dashti S, Ghofrani A, Taiebat M, et al. Site response in a layered liquefiable deposit: evaluation of different numerical tools and methodologies with centrifuge experimental results. J Geotech Geoenviron Eng 2018;144(10):04018073.

[34] Ghofrani A, Arduino P. Prediction of LEAP centrifuge test results using a pressure-dependent bounding surface constitutive model. Soil Dyn Earthq Eng 2018;113:757–70.

[35] Reyes A, Adinata J, Taiebat M. Impact of bidirectional seismic shearing on the volumetric response of sand deposits. Soil Dyn Earthq Eng 2019;125:105665.

[36] Li X-S, Dafalias YF. Anisotropic critical state theory: role of fabric. J Eng Mech 2012;138(3):263–75.

[37] Dafalias YF, Taiebat M. SANISAND-Z: zero elastic range sand plasticity model. Géotechnique 2016;66(12):999–1013.

[38] Petalas AL, Dafalias YF, Papadimitriou AG. SANISAND-FN: An evolving fabric-based sand model accounting for stress principal axes rotation. Int J Numer Anal Methods Geomech 2018;43(1):97–123.

[39] Petalas AL, Dafalias YF, Papadimitriou AG. SANISAND-F: Sand constitutive model with evolving fabric anisotropy. Int J Solids Struct 2020;188–189:12–31.
[40] Medicus G, Taiebat M. Animating soil models: SANISAND. 2022, URL https://soilmodels.com/soilanim/#link_tab-1609524430349-10, (Accessed: 2022-12-01).
[41] Corti R, Diambra A, Wood DM, Escribano DE, Nash DFT. Memory surface hardening model for granular soils under repeated loading conditions. J Eng Mech 2016;142(12):04016102.
[42] Liu HY, Abell JA, Diambra A, Pisanó F. Modelling the cyclic ratcheting of sands through memory-enhanced bounding surface plasticity. Géotechnique 2019;69(9):783–800.
[43] Barrero AR, Taiebat M, Dafalias YF. Modeling cyclic shearing of sands in semifluidized state. Int J Numer Anal Methods Geomech 2020;44(3):371–88.
[44] Kutter BL, Manzari MT, Zeghal M, editors. Model tests and numerical simulations of liquefaction and lateral spreading: LEAP-UCD-2017. Springer; 2020.
[45] Vasko A. An investigation into the behavior of Ottawa sand through monotonic and cyclic shear tests. (Master's thesis), Washington, USA: The George Washington University; 2015.
[46] Bastidas AMP. Ottawa F-65 sand characterization (Ph.D. thesis), Davis, CA, USA: Department of Civil and Environmental Engineering, University of California; 2016.
[47] Ghoraiby ME, Manzari MT. Stress-strain behavior and liquefaction strength characteristics of Ottawa F65 sand, Soil Dyn Earthq Eng 138, 106292.
[48] El Ghoraiby M, Manzari MT. Cyclic behavior of sand under non-uniform shear stress waves. Soil Dyn Earthq Eng 2021;143:106590.
[49] Reyes A, Yang M, Barrero AR, Taiebat M. Numerical modeling of soil liquefaction and lateral spreading using the SANISAND-Sf model in the LEAP experiments. Soil Dyn Earthq Eng 2021;143:106613.
[50] Zeghal M. LEAP-RPI 2020: Version 0.91 model specifications. 2019.
[51] Korre E, Abdoun T, Zeghal M. Repeatability potential and challenges in centrifuge physical modeling in the presence of soil-structure interaction for LEAP-2020. In: Wang L, Zhang J-M, Wang R, editors. Proceedings of the 4th international conference on performance based design in earthquake geotechnical engineering (Beijing 2022). Cham: Springer International Publishing; 2022, p. 1794–801.
[52] Guan X, Fusco A, Haigh SK, Madabhushi GSP. LEAP-2021 cambridge experiments on cantilever retaining walls in saturated soils. In: Wang L, Zhang J-M, Wang R, editors. Proceedings of the 4th international conference on performance based design in earthquake geotechnical engineering (Beijing 2022). Cham: Springer International Publishing; 2022, p. 1785–93.
[53] Wang Y-H, Huang J-X, Lin Y-H, Hung W-Y. Centrifuge modeling on the behavior of sheet pile wall subjected different frequency content shaking. In: Wang L, Zhang J-M, Wang R, editors. Proceedings of the 4th international conference on performance based design in earthquake geotechnical engineering (Beijing 2022). Cham: Springer International Publishing; 2022, p. 1829–36.
[54] Manandhar S, Lee S-R, Cho G-C. Rotation of a cantilevered sheet-pile wall with different embedment ratios and retaining a liquefiable backfill of various relative densities. In: Wang L, Zhang J-M, Wang R, editors. Proceedings of the 4th international conference on performance based design in earthquake geotechnical engineering (Beijing 2022). Cham: Springer International Publishing; 2022, p. 1144–51.
[55] Basu D, Pretell R, Montgomery J, Ziotopoulou K. Investigation of key parameters and issues in simulating centrifuge model tests of a sheet-pile wall retaining a liquefiable soil deposit. Soil Dyn Earthq Eng 2022;156:107243.
[56] Perez K, Reyes A, Taiebat M. Numerical modeling of the LEAP-RPI-2020 centrifuge tests using the SANISAND-MSf model in FLAC3D. In: Wang L, Zhang J-M, Wang R, editors. Proceedings of the 4th international conference on performance based design in earthquake geotechnical engineering (Beijing 2022). Cham: Springer International Publishing; 2022, p. 1802–11.
[57] Qiu Z, Elgamal A. Numerical simulations of LEAP centrifuge experiments using a multi-surface cyclic plasticity sand model. In: Wang L, Zhang J-M, Wang R, editors. Proceedings of the 4th international conference on performance based design in earthquake geotechnical engineering (Beijing 2022). Cham: Springer International Publishing; 2022, p. 1812–20.
[58] Chen L, Ghofrani A, Arduino P. Lessons learned from LEAP-RPI-2020 simulation practice. In: Wang L, Zhang J-M, Wang R, editors. Proceedings of the 4th international conference on performance based design in earthquake geotechnical engineering (Beijing 2022). Cham: Springer International Publishing; 2022, p. 1763–71.
[59] He B, Zhang J, Li W, Wang R. Numerical analysis of LEAP centrifuge tests on sloping liquefiable ground: Influence of dilatancy and post-liquefaction shear deformation. Soil Dyn Earthq Eng 2020;137:106288.
[60] Chen L, Ghofrani A, Arduino P. Remarks on numerical simulation of the LEAP-Asia-2019 centrifuge tests. Soil Dyn Earthq Eng 2021;142:106541.
[61] Ishihara K, Yasuda S. Sand liquefaction in hollow cylinder torsion under irregular excitation. Soils Found 1975;15(1):45–59.
[62] Wang JN, Kavazanjian EJ. Pore pressure development during non-uniform cyclic loading. Soils Found 1989;29(2):1–14.
[63] Kramer SL, Sideras SS. Transient loading effects on pore pressure generation and the response of liquefiable soils. In: Wang L, Zhang J-M, Wang R, editors. Proceedings of the 4th international conference on performance based design in earthquake geotechnical engineering (Beijing 2022). Cham: Springer International Publishing; 2022, p. 74–99.
[64] Kramer SL, Sideras SS, Greenfield MW. The timing of liquefaction and its utility in liquefaction hazard evaluation. Soil Dyn Earthq Eng 2016;91:133–46.
[65] Ozener PT, Greenfield MW, Sideras SS, Kramer SL. Identification of time of liquefaction triggering. Soil Dyn Earthq Eng 2020;128:105895.
[66] CDA. Dam safety guidelines 2007 (2013 edition). Canadian Dam Association; 2013, ISBN 978-0-9936319-0-0.
[67] Taiebat M, Shahir H, Pak A. Study of pore pressure variation during liquefaction using two constitutive models for sand. Soil Dyn Earthq Eng 2007;27(1):60–72.
[68] Shahir H, Pak A, Taiebat M, Jeremić B. Evaluation of variation of permeability in liquefiable soil under earthquake loading. Comput Geotech 2012;40:74–88.
[69] Dashti S, Bray JD, Pestana JM, Riemer MF, Wilson D. Centrifuge testing to evaluate and mitigate liquefaction-induced building settlement mechanisms. J Geotech Geoenviron Eng 2010;136(7):918–29.
[70] Bray JD, Macedo J. 6th Ishihara lecture: Simplified procedure for estimating liquefaction-induced building settlement. Soil Dyn Earthq Eng 2017;102:215–31.
[71] Tokimatsu K, Asaka Y. Effects of liquefaction-induced ground diplacements on pile performance in the 1995 Hyogoken-Nambu earthquake. Soils Found 1998;38:163–77.
[72] Takashahi A, Takemura J. Liquefaction-induced large displacement of pile-supported wharf. Soil Dyn Earthq Eng 2005;25:811–25.
[73] Chen R, Taiebat M, Wang R, Zhang J-M. Effects of layered liquefiable deposits on the seismic response of an underground structure. Soil Dyn Earthq Eng 2018;113:124–35.
[74] Zhu T, Wang R, Zhang J-M. Effect of nearby ground structures on the seismic response of underground structures in saturated sand. Soil Dyn Earthq Eng 2021;146:106756.
[75] Karimi Z, Dashti S, Bullock Z, Porter K, Liel A. Key predictors of structure settlement on liquefiable ground: a numerical parametric study. Soil Dyn Earthq Eng 2018;113:286–308.
[76] Bullock Z, Karimi Z, Dashti S, Porter K, Liel AB, Franke KW. A physics-informed semi-empirical probabilistic model for the settlement of shallow-founded structures on liquefiable ground. Géotechnique 2019;69(5):406–19.